



1 **Petrogenesis and tectonic setting of late Paleoproterozoic diorites in the**

2 **Trans-North China Orogen**

3

4 Zhiyi Wang ^{a, b}, Jun He ^{a*}, Wolfgang Siebel ^b, Shuhao Tang ^a, Yiru Ji ^a, Jianfeng He ^a, Fukun Chen ^a

5

6

7 a: State Key Laboratory of Lithospheric and Environmental Coevolution, School of Earth and

8 Space Sciences, University of Science and Technology of China, Hefei 230026, China

9 b: Institute of Earth and Environmental Sciences, Albert-Ludwig University Freiburg, Freiburg

10 79104, Germany

11

12

13 *Corresponding author: jhe1989@ustc.edu.cn (J. He)

14

15



16 **Abstract:** The Xiong'er volcanic rocks and mafic dike swarms mark a significant
17 magmatic event after the amalgamation of the North China Craton (NCC) in the
18 Paleoproterozoic, yet their tectonic origins remain controversial. Several
19 Paleoproterozoic diorite intrusions have received widespread attention recently. Their
20 genesis and geological significance are crucial for understanding the evolution of the
21 NCC. In this study, we report zircon U-Pb ages and geochemical data of the
22 Jiguanshan diorite. The diorites in the Trans-North China Orogen, including the
23 Jiguanshan diorite, have comparable element and isotopic geochemical characteristics.
24 The weighted mean average of initial $^{87}\text{Sr}/^{86}\text{Sr}$ and $\epsilon_{\text{Nd}}(t)$ values is 0.7052 ± 0.0003
25 and -6.5 ± 0.2 , respectively. The initial Pb isotope compositions of these diorite
26 samples do not show significant enrichment of radiogenic lead. In terms of Sr-Nd-Pb
27 isotope compositions and Nb/Ta, Ba/Th, and Sr/Th ratios, these diorites differ from
28 the Xiong'er volcanic rocks and mafic dike swarms. Our results suggest that these
29 diorites originated from the basaltic lower crust, rather than from the enriched
30 subcontinental lithospheric mantle. Whole-rock and zircon trace element geological
31 tectonic diagrams indicate that the diorites formed in a rift environment. These
32 diorites mark a crustal-origin rock shift from orogenic-related magmatism to
33 intraplate magmatism during the post-collisional extensional stage.

34
35 **Key words:** Late Paleoproterozoic, North China, Diorite, Zircon, Sr-Nd-Pb isotopes

36



37 **1 Introduction**

38 The ancient basement rocks in the North China Craton (NCC) provide crucial insights
39 into the Precambrian geological evolution (e.g., [Geng et al., 2012](#); [Liu et al., 1992](#)).
40 The main assembly of the NCC took place after the collision of eastern and western
41 land masses in the late Paleoproterozoic (e.g., [Zhao and Zhai, 2013](#); [Zhao et al., 2000a](#),
42 [b](#)). Subsequently, the craton experienced multiple rift phases, with the Xiong'er rift
43 being the first rift formed after the assembly, resulting in the formation of the *c.* 1780
44 Ma Xiong'er volcanic rocks and contemporaneous mafic dyke swarms (e.g., [Hou et](#)
45 [al., 2008](#); [Peng et al., 2007, 2008](#); [Zhai, 2010](#)). However, the origin and tectonic
46 setting of the Xiong'er volcanic rocks and contemporaneous mafic dyke swarms of
47 the NCC remains controversial. The debate mainly revolves around subduction (e.g.,
48 [He et al., 2009](#); [Wang et al., 2004](#); [Zhao et al., 2009](#)), rifting (e.g., [Cui et al., 2010](#);
49 [Zhao et al., 2007](#)), and the involvement of mantle plumes (e.g., [Hou et al., 2008](#); [Peng](#)
50 [et al., 2007, 2008](#)). Clarifying the tectonic setting during this period is essential for
51 understanding the post-collisional orogenic evolution that followed the late
52 Paleoproterozoic amalgamation of the North China Craton.

53 In recent years, numerous *c.* 1780 Ma diorites along the southern margin of the NCC
54 and the Shanxi region ([Fig. 1a](#)) have attracted significant attention, potentially
55 offering new perspectives for understanding the tectonic evolution of the craton
56 during the late Paleoproterozoic. These rocks include the diorites intruding into the
57 Xushan Formation (ca. 1789 Ma; [Zhao et al., 2004](#)), the East-West Group dykes (ca.
58 1780 Ma; [Peng et al., 2007](#)), the Shizhaigou diorite (ca. 1780 Ma; [Cui et al., 2011](#)),
59 the Wafang diorite (ca. 1750 Ma; [Wang et al., 2016](#)), the Gushicun diorite (ca. 1780
60 Ma; [Ma et al., 2023a](#)), the Muzhijie diorite (ca. 1780 Ma; [Ma et al., 2023b](#)), the
61 Fudian diorite (ca. 1780 Ma; [Ma et al., 2023b](#)), and the Jiguanshan diorite (ca. 1780



Ma; this study). These diorites are widely distributed, with similar zircon ages and an approximate east-west trend. Some studies suggest some of them share a source with the Xiong'er Group volcanic rocks or dyke swarms, formed by fractional crystallization of enriched mantle (Cui et al., 2011; Peng et al., 2007). Others propose some of them resulted from the fractional crystallization (Ma et al., 2023a, b) or crustal melting with limited mantle influence (Wang et al., 2016). Systematic research into their genesis is crucial for clarifying their formation and constraining regional geological evolution.

The present study focuses on the Jiguanshan diorite and other diorites with ages of *c.* 1.78–1.75 Ga from the NCC. These diorites have similar geochemical characteristics, suggesting they may have formed during a single magmatic episode. By evaluating the geochemical and Sr-Nd-Pb isotopic compositions of whole rocks, as well as Hf isotopic compositions of zircons, a better understanding of the tectonic environment and evolution of the NCC during the late Paleoproterozoic is provided.

76

77 **2 Geological background and samples**

The NCC records a 3.8 Ga lasting geological evolution (e.g., Geng et al., 2012; Liu et al., 1992). It was ultimately formed by the assembly of the eastern and western blocks along the central orogenic belt at the end of the Paleoproterozoic (e.g., Zhao and Zhai, 2013; Zhao et al., 2000a, b). The southern margin of the NCC is mainly occupied by the “Xiong'er rift”, which is separated from the North Qinling Orogen by the Luonan–Luanchuan fault (Fig. 1b). Before the Mesozoic, the southern margin of the NCC experienced a similar geological evolution as the NCC itself, which makes it an ideal object for studying the Precambrian geological evolution (e.g., Zhai, 2010).

The study area is located in the eastern part of the southern margin of the NCC (Fig.



87 [1b](#)). The most frequent basement rocks in this area are metamorphic basement rocks
88 of the Archean Taihua Group. The Taihua Group extends in an east-west direction
89 from Lantian in the west to Wuyang in the east (e.g., [Diwu et al., 2014, 2018](#); [Wang et](#)
90 [al., 2020](#)). The upper part of the basement contains volcanic rocks of the Xiong'er
91 Group that formed *c.* 1780 Ma (e.g., [Zhao et al., 2004, 2007](#)). The Xiong'er volcanic
92 rocks consist mainly of basalts and andesites that are widely distributed along the
93 southern margin of the NCC, and extend as far north as Taiyuan City in Shanxi
94 Province ([Zhao et al., 2007](#)). The Xiong'er Group represents the largest magmatic unit
95 of the NCC since the Neoproterozoic period. At the same time, a large mafic dyke swarm
96 emplaced the NCC. These mafic rocks are interpreted as products of crustal extension
97 during the Columbia supercontinent era (e.g., [Peng et al., 2008](#); [Wang et al., 2004](#)).

98 During our fieldwork, seven diorite samples were collected from the Jiguanshan
99 diorite on the eastern side of the Jiguanshan Hill (or the Jiguan Mountain), about 30
100 km south of Ruyang County, Henan Province ([Fig. 1c](#) and [Table S1](#)). The Jiguanshan
101 diorite forms several east-west striking bodies that are cut by the Mesozoic
102 Taishanmiao A-type granite to the west. The Taishanmiao intrusion, located at the
103 southern margin of the NCC in the western Henan region, covers an area of *c.* 290
104 km² (e.g., [He et al., 2021](#)). The northern and eastern part of the Taishanmiao intrusion
105 penetrates the volcanic rocks of the Xiong'er Group ([Fig. 1c](#)).

106 The collected samples of Jiguanshan diorite are fresh and greyish with massive
107 structures. They are fine-grained with a particle size of 0.1–2 mm ([Fig. 2a, b](#)). The
108 main mineral is plagioclase (~60 vol.%), which varies greatly in size and has a
109 lamellar and euhedral shape. Under the microscope, the partially sericitized crystals
110 show simple contact twinning and polysynthetic twinning. Some plagioclase crystals
111 show zonal and resorption textures ([Fig. 2c-e](#)) and the Carlsbad-Albite composite twin



112 with zoned texture (Fig. 2d). Clinopyroxene (~15 vol.%) formed earlier than
113 plagioclase. Most of the clinopyroxenes have zonal and resorption textures (Fig. 2f).
114 Euhedral opaque minerals (~3 vol.%), such as ilmenite, are often encased in
115 clinopyroxene. Alkaline feldspar (~10 vol.%) shows hypidiomorphic to xenomorphic
116 texture with imprints of kaolinization (Fig. 2c, e). The mineral occurs as potassium
117 feldspar and perthite. Quartz (~5 vol.%) can also appear as an anhedral crystal. Biotite
118 (~3 vol.%) shows xenomorphic texture or is altered into chloride (Fig. 2c, e). In
119 addition, accessory minerals such as zircon and ilmenite account for about 3 vol.%
120 (Fig. 2f).

121

122

123 **3 Method**

124 **Major and trace elements:** Seven representative fresh rock samples were selected to
125 be broken up into powders less than 200 mesh. Major element composition of whole
126 rock was obtained by X-ray fluorescence (XRF) from ALS Chemex (Guangzhou)
127 using a PANalytical PW2424 instrument. Following the sample digestion, whole-rock
128 trace element concentrations were determined using an Agilent 7700 inductively
129 coupled plasma mass spectrometry (ICP-MS) at the University of Science and
130 Technology of China (USTC). Quality control assurance was achieved by using GSR–
131 1, BCR–2, and AGV–2. The analytical uncertainties are <5%.

132 **Whole-rock Sr-Nd-Pb isotopes:** Chemical separation of whole-rock Sr-Nd-Pb
133 isotope analysis was performed in the ultra-clean laboratory of the Laboratory of
134 Radiogenic Isotope Geochemistry, USTC. Whole-rock powders of *c.* 100 mg were
135 weighed in 7 ml Teflon cups in a solution of purified HF and HNO₃ acids for Pb



136 isotopic analysis and in a solution of purified HF and HClO₄ acids for Sr-Nd isotopic
137 analysis. Sr and Nd were separated by AG 50W-X12 resin in 200–400 mesh purposes
138 and purified using the Sr-Spec[®] ion-exchange resin for Sr and Ln-Spec[®] resin for Nd.
139 All isotopic measurements were done on a Triton Plus mass spectrometer of Thermo
140 Scientific[™]. Measured Sr and Nd ratios were normalized to $^{86}\text{Sr}/^{88}\text{Sr} = 0.1194$ and
141 $^{143}\text{Nd}/^{144}\text{Nd} = 0.7219$, respectively. Pb isotope ratios were corrected for mass
142 fractionation using a fractionation factor of 0.1% per atomic mass unit based on
143 repeated measurements of reference material NIST NBS 981 (Wang et al., 2023a).
144 Total procedure blanks for Sr, Nd, and Pb were <200 pg. Detailed procedures can be
145 found elsewhere (Chen et al., 2000, 2007). The errors of the initial values of Sr and
146 Nd isotopes were obtained by the error transfer formula, which is shown in Table 2 for
147 Sr and Table 3 for Nd. Detailed formulas can be found in Siebel et al. (2005). A 5%
148 age error, a 2‰ $^{87}\text{Rb}/^{86}\text{Sr}$ measurement error, and a 0.3‰ $^{87}\text{Sr}/^{86}\text{Sr}$ measurement error
149 were used for the error of initial Sr values for calculation. A 5% age error, a 0.3‰
150 $^{147}\text{Sm}/^{143}\text{Nd}$ error, and the $^{143}\text{Nd}/^{144}\text{Nd}$ measurement error were used for the
151 calculation of the error of initial Nd isotope values.

152 **Zircon U-Pb age and trace elements:** Zircon crystals were isolated from the rocks
153 by standard mineral separation procedures. Grains with intact crystal shape and no
154 obvious inclusions were selected under a binocular microscope. The zircons were
155 embedded in epoxy resin. The upper and lower planes of each zircon target were
156 polished with sandpaper from coarse to fine. Most of the zircon grains were polished to
157 2/3 of the position and then cleaned in ultra-pure water by ultrasonic waves. The
158 grains were cleaned with dust-free paper in a certain direction to ensure that the zircon
159 was clean and bright without impurities under the microscope for carbon plating.
160 Cathodoluminescence (CL) image analysis was done on a scanning electron



161 microscope (SEM) located at the USTC. Zircon U-Pb isotopic and trace element
162 compositions were obtained by laser-ablation inductively-coupled plasma mass
163 spectrometry (LA-ICP-MS) using an Agilent 7700 ICP-MS with a 193 nm ArF
164 laser-ablation system at the USTC. The beam spot diameter was 32 μm , operating at a
165 repetition rate of 10 Hz. Helium served as the carrier gas. Zircon 91500 was used as a
166 standard for age calculation. The NIST SRM 610 and 612 were utilized as reference
167 materials for content adjustment. U-Pb ratios and uranium and lead concentration data
168 were calculated by the ICPMSDataCal software (Liu et al., 2010). Concordia and
169 weighted mean age plots were made using IsoplotR (Vermeesch, 2018).

170

171 **4 Analytical results**

172 Whole-rock compositions of the Jiguanshan diorite are given in Table 1, and
173 Sr-Nd-Pb isotope compositions and error calculations are shown in Tables 2 to 4. Age
174 results of zircon grains from four samples are given in Table S1, and trace elemental
175 contents in Table S2.

176

177 **4.1 Zircon U–Pb isotopic ages**

178 Zircon grains from the Jiguanshan diorite are transparent to pale yellow with
179 subhedral to euhedral habitus. They measure *c.* 100–300 μm in length and have aspect
180 ratios of 1:1 to 3:1. Most of them show oscillatory zoning in the CL images (Fig. 3),
181 which suggests their magmatic origin.

182 Twenty-nine zircon grains from sample ZY2202 yield $^{207}\text{Pb}/^{206}\text{Pb}$ ages varying from
183 1885 ± 44 Ma to 1643 ± 42 Ma and giving a weighted mean age of 1772 ± 16 Ma (2σ ,
184 $n=29$, Fig. 4a). Thirty-two zircon grains from sample ZY2204 yield $^{207}\text{Pb}/^{206}\text{Pb}$ ages



185 varying from 1902 ± 54 Ma to 1635 ± 47 Ma with a weighted mean age of 1742 ± 15
186 Ma (2σ , $n=32$, Fig. 4b). Twenty-six out of twenty-seven zircon grains from sample
187 ZY2205 yield $^{207}\text{Pb}/^{206}\text{Pb}$ ages varying from 1933 ± 52 Ma to 1692 ± 44 Ma and a
188 weighted mean age of 1760 ± 18 Ma (2σ , $n=26$, Fig. 4c). One zircon has a $^{207}\text{Pb}/^{206}\text{Pb}$
189 age of 1639 ± 46 Ma (96% concordance), which is excluded from the calculation (Fig.
190 4c). Thirty zircon grains of sample ZY2207 yield $^{207}\text{Pb}/^{206}\text{Pb}$ ages ranging from 1900
191 ± 54 Ma to 1700 ± 36 Ma with a weighted mean age of 1771 ± 17 Ma (2σ , $n=30$, Fig.
192 4d).

193 Most zircon grains have Th/U ratios >1 , supporting their magmatic origin (Table S1).
194 Some grains deviate from the concordant line, which is related to lead loss (Fig. 4a-d).
195 The weighted mean ages of the Jiguanshan diorite near 1780 Ma suggest that the
196 diorite body formed in the late Paleoproterozoic.

197

198 4.2 Whole-rock chemical composition

199 The SiO_2 contents of the Jiguanshan diorite vary between 55.57 and 59.44 wt. % and
200 the sum of $\text{K}_2\text{O}+\text{Na}_2\text{O}$ from 5.57 to 6.03 wt. %, corresponding to gabbroic diorite to
201 diorite composition according to the TAS diagram (Fig. 5a). K_2O contents range from
202 2.97 to 3.21 wt. % and fall within the high-K calc-alkaline fields (Fig. 5b). The
203 samples from the Jiguanshan diorite have consistent A/CNK ratios ranging from 0.78
204 to 0.81 and A/NK >1 , which classify them as metaluminous rocks (Fig. 5c). $\text{Mg}^\#$
205 ($\text{Mg}^\#=(\text{MgO}+\text{FeO}_{\text{total}})/\text{MgO} \times 100$) values range from 34 to 39 (Fig. 5d).

206 The Jiguanshan diorite depicts the enrichment of large ion lithophile elements (LILE),
207 such as Rb, Ba, and K, and negative anomalies of Sr, Ti, Nb, and Ta (Fig. 6a). $\sum\text{REE}$
208 contents range from 361 ppm to 393 ppm. Light rare earth elements (LREE) exhibit



209 stronger enrichment, while heavy rare earth elements (HREE) are relatively depleted
210 (Fig. 6b). Their $(La/Yb)_N$ ratios range from 12.2 to 15.0 (subscript N denotes
211 normalization against chondrite La and Yb contents) with Eu/Eu^*
212 ($Eu/Eu^* = 2Eu_N/(Sm_N + Gd_N)$, subscript N denotes normalization against chondrite Sm
213 and Gd contents) ratios ranging from 0.57 to 0.68 (Table 1).

214

215 4.3 Whole-rock Sr-Nd-Pb isotopic compositions

216 All initial radiogenic isotopic values and the errors of the initial values of Sr, Nd and
217 Pb isotopes are calculated back to an age of 1780 Ma. The measured $^{87}Sr/^{86}Sr$ isotope
218 compositions of Jiguanshan diorite samples vary from 0.715177 ± 0.000011 to
219 0.724714 ± 0.000012 (2σ). Initial Sr ratios range from 0.7020 ± 0.0007 to 0.7058
220 ± 0.0010 (2σ , Fig. 7a). Measured $^{143}Nd/^{144}Nd$ values vary from 0.511129 ± 0.000008 to
221 0.511329 ± 0.000007 (2σ). Initial $^{143}Nd/^{144}Nd$ isotope compositions range from
222 0.509924 ± 0.000061 to 0.510090 ± 0.000063 (2σ), corresponding to initial ϵ_{Nd} values
223 of -8.04 ± 1.20 to -4.80 ± 1.23 (2σ , Fig. 7b) and two-stage Nd model ages (T_{DM2}) of
224 2.94 Ga to 2.68 Ga. Their Pb isotopic compositions are as follows: $^{206}Pb/^{204}Pb =$
225 $15.832\text{--}16.167$, $^{207}Pb/^{204}Pb = 15.170\text{--}15.243$, and $^{208}Pb/^{204}Pb = 36.046\text{--}37.324$. Initial
226 Pb isotope ratios are significantly lower: $^{206}Pb/^{204}Pb_i$ ratios ranging from 14.965 to
227 15.295 , $^{207}Pb/^{204}Pb_i$ ratios ranging from 15.090 to 15.150, $^{208}Pb/^{204}Pb_i$ ratios ranging
228 from 34.398 to 35.825, with $^{238}U/^{204}Pb$ and $^{232}Th/^{238}U$ ratios ranging from 2.3 to 2.9
229 and 5.3 to 7.8, respectively (Fig. 8a, b).

230

231 5 Discussion

232 5.1 Compositional characteristics of late-Paleoproterozoic diorites of the NCC



233 The late Paleoproterozoic diorites in the NCC have uniform east-west (EW) strike,
234 suggesting a possible correlation, which differs from the north-northwest (NNW)
235 strike of most contemporaneous mafic dykes (Hou et al., 2008; Peng et al., 2007,
236 2008). The intrusion ages of these diorites are concentrated between 1780 and 1750
237 Ma. All the diorites have similar geochemical and isotopic compositions and can be
238 regarded as a compositional homogeneous rock group.

239 Summarizing the late-Paleoproterozoic diorites of the NCC, most of them have SiO₂
240 contents in the range of 52–62 wt. % (Fig. 5a). Total alkali content (K₂O+Na₂O) of 5–
241 7 wt. % suggests a subalkaline character for the diorite rocks (Fig. 5a). The K₂O
242 contents of these samples range from 2–5 wt. % in accordance with a high-K
243 calc-alkaline to shoshonite series (Fig. 5b). The ASI and Mg[#] values of these samples,
244 except for a few data points that deviate significantly, are mostly homogeneous, with
245 weighted average values of 0.81 and 37, respectively (Fig. 5c, d). On primitive mantle
246 normalization diagrams, all the diorites display enrichment of large ion lithophilic
247 elements (LILEs), such as Rb, Ba, and K, and depletion of high field strength
248 elements (HFSEs), such as Na, Ta, Th, U, and Ti (Fig. 6). On the rare earth element
249 normalization diagrams, they have negative Eu anomalies with enrichment in LREEs
250 and flat distribution of HREEs (Fig. 6). As can be seen from the above, the oxides and
251 trace elements of these diorites have similarities.

252 All diorites have similar Nd isotopic compositions with the mean initial ϵ_{Nd} value of
253 -6.51 ± 0.2 (2σ , $n=41$, Fig. 7b), when we recalculate the initial ϵ_{Nd} values and their
254 errors back to 1780 Ma using the data from previous studies (Table 3). The overall
255 range of initial ϵ_{Nd} values is from -10.2 ± 1.21 to -4.80 ± 1.23 (2σ , Fig. 7b). Some
256 samples from Wafang diorite (namely Muzhijie diorite in some literatures, Ma et al,
257 2023b; Wang et al, 2016) have enriched Nd isotope composition, which may be



258 explained by assimilation or contamination of the continental crust due to their higher
259 zirconium contents (Fig. 7b; Table 3). Overall, the initial ϵ_{Nd} values and the
260 corresponding two-stage Nd model ages (T_{DM2}) of the late Paleoproterozoic diorites
261 are consistent with each other except for the Wafang diorite (Table 3).

262 The initial ϵ_{Hf} values of zircons from the diorites in the NCC have a wide but
263 consistent range of variations: from -17 to -2.5 in the Gushicun diorite (Ma et al,
264 2023a; Fig. 7c), from -14 to 0.55 in the Muzhijie diorite (Ma et al, 2023b; Fig. 7c),
265 and from -17 to 0.95 in the Fudian diorite (Ma et al., 2023b; Fig. 7c). In summary, the
266 diorites in the NCC have similar Nd-Hf isotopic compositions and form a coherent
267 group in geochemical diagrams, indicating a close genetic relationship.

268

269 **5.2 Initial Sr isotope composition and magma source**

270 The late Paleoproterozoic diorites in the NCC show a large range in whole-rock initial
271 Sr isotopic compositions (Fig. 7a; Jiguanshan diorite: 0.7020 to 0.7058; Wafang
272 diorite: 0.7004 to 0.7050; Shizhaigou diorite: 0.7005 to 0.7053; East-West group dikes:
273 0.7011 to 0.7053). Determining magma sources for rocks with widely varying initial
274 Sr ratios is complex, as Sr isotopes can be affected by magma mixing, assimilation,
275 contamination, and melting degrees. (e.g., Gao et al., 2015; Wolf et al., 2019; Zeng et
276 al., 2005).

277 The whole-rock Nd isotopic compositions suggest a heterogeneous magma source
278 without mixing with the mantle (Fig. 7b). On the other hand, mantle-derived rocks
279 often have a high MgO content and elevated levels of compatible elements such as Ni
280 and Cr, which are inconsistent with the elemental content characteristics of these
281 diorites (Table 1, see previous references).



282 Variability in Sr isotopic compositions can result from different degrees of source
283 melting. However, a mica- and feldspar-rich source with high Rb/Sr ratios produces
284 melts with more radiogenic $^{87}\text{Sr}/^{86}\text{Sr}$ ratios (e.g., [Hu et al., 2018](#)). Melts affected by
285 the dehydration of amphibole typically have low $^{87}\text{Sr}/^{86}\text{Sr}$ ratios with adakitic
286 characteristics (e.g., [Rapp and Watson, 1995](#); [Wolf et al., 1993](#)). The different degrees
287 of source melting are unlikely to be the main cause.

288 The initial $^{87}\text{Sr}/^{86}\text{Sr}$ values negatively correlate with the $^{87}\text{Rb}/^{86}\text{Sr}$ ratios when they are
289 less than 0.704 ([Fig. 7a](#)). When the initial $^{87}\text{Sr}/^{86}\text{Sr}$ values are greater than 0.704, such
290 correlation no longer exists. The large uncertainty propagation in calculating the
291 initial whole-rock Sr isotope compositions for old samples may be the main factor. All
292 diorites have samples with the initial $^{87}\text{Sr}/^{86}\text{Sr}$ values greater than 0.704. Excluding
293 outliers, the mean average initial $^{87}\text{Sr}/^{86}\text{Sr}$ value is 0.7052 ± 0.0003 (2σ , $n=8$), which
294 might represent the most likely initial Sr isotopic composition of the source ([Fig. 7a](#)).

295 The initial Sr isotopic compositions of the Xiong'er Group rocks vary widely and tend
296 to have more variable and radiogenic Sr isotopic ratios ([Fig. 7d](#)). The initial Sr isotope
297 compositions of these diorites are much similar to the lower crustal Archean xenoliths
298 from the southeastern NCC (initial $^{87}\text{Sr}/^{86}\text{Sr}$ values: 0.7039–0.7068, $t=1780$ Ma, e.g.,
299 [Huang et al., 2004](#)), suggesting that they are more likely associated with lower crustal
300 rocks in the NCC rather than an enriched mantle source like the Xiong'er Group.

301

302 **5.3 Petrogenetic considerations**

303 Several hypotheses have been proposed for the petrogenesis of intermediate dioritic
304 rocks including partial melting of metasomatized mantle (e.g., [Chen et al., 2021](#)),
305 partial melting of subducted oceanic crust and subsequent melt-peridotite reaction



(e.g., Kelemen, 1995; Stern and Kilian, 1996), magma mixing/mingling (e.g., Reubi and Blundy, 2009; Streck et al., 2007), melting of basaltic rocks (e.g., Jackson et al., 2003; Petford and Atherton, 1996), fractional crystallization of basaltic magmas (e.g., Castillo et al., 1999).

The diorites from the NCC have similar MgO and low compatible element contents, suggesting that they were not derived directly from a mantle magma source (Fig. 9a). The magma mixing/mingling with mantle can also be excluded due to their homogeneous initial Nd isotope compositions (Fig. 7b), and consistent SiO₂ contents and Mg[#] values (Fig. 5d).

Partial melting of the oceanic crust in the subducted slab can also form intermediate rocks, such as adakites, which often exhibit high Sr/Y ratios (>20) and low Y contents (<18 ppm) (e.g., Defant and Drummond, 1990; Peacock et al., 1994). The Jiguanshan and other diorites from the NCC have relatively high Y and Sr contents with Sr/Y ratios <15. Thus, partial melting of the oceanic crust does not appear to be the reason for these diorites.

As can be seen from the Harker variation diagrams, the Cr contents decrease with decreasing MgO, indicating fractionation of clinopyroxene (Fig. 9a). The CaO contents decrease with increasing SiO₂, suggesting crystallization of minerals, such as plagioclase or clinopyroxene (Fig. 9b). However, Al₂O₃ and Na₂O contents do not significantly decrease with increasing SiO₂, indicating that plagioclase and clinopyroxene were not significant fractionation phases (Fig. 9c-d). The increase in K₂O contents with increasing SiO₂ suggests no biotite and/or K-feldspar fractionation during magmatic evolution (Fig. 9e). The increasing SiO₂ and decreasing TiO₂ indicate the crystallization and fractionation of Ti-bearing minerals, such as ilmenite (Fig. 9f). The Eu/Eu* values of the diorites do not show significant changes with Sr



331 contents, which also proves that fractionation of plagioclase from the melt was not
332 significant (Fig. 9g). From the above discussion, it can be concluded that the
333 petrogenesis of the diorites in the NCC was associated with minor fractional
334 crystallization processes. Whole-rock La/Yb versus La and Zr/Sm versus Zr
335 correlations are as expected for a partial melting process (Fig. 9h-i). This implies that
336 the formation of the diorites may be closely related to the partial melting of a basaltic
337 protolith.

338 The basement rocks of the lower Taihua Group in the southern margin of the NCC
339 consist of amphibolite (e.g., Diwu et al., 2014, 2018; Wang et al., 2020). Partial
340 melting of amphibolite can also lead to the production of intermediate to acidic
341 magmas (e.g., Beard and Lofgren, 1991; Rapp and Watson, 1995). The amphibolites
342 of the Taihua Group are characterized by low K content and low K₂O/Na₂O ratios
343 (<0.5, Wang et al., 2019), making it difficult to generate high-K₂O rocks. (Beard and
344 Lofgren, 1991; Roberts and Clemens, 1993). The partial melting of amphibolite
345 typically produces peraluminous melts (e.g., Beard and Lofgren, 1991; Rapp and
346 Watson, 1995), whereas the diorites in the NCC have low Al₂O₃ content with
347 metaluminous character (Fig. 5c; weight average A/NCK values of 0.81). Additionally,
348 the ϵ_{Nd} values of the Taihua Group amphibolites at t=1780 Ma show a wide range
349 from -6.7 to 0.4, which is inconsistent with those of the diorites (Wang et al., 2019).
350 Therefore, it seems unlikely that the diorites formed by the partial melting of Taihua
351 Group amphibolites.

352 The mafic rocks in the Xiong'er Group or the mafic dyke swarms are believed to be
353 the origin of the diorites. (Cui et al., 2011; Ma et al., 2023b; Peng et al., 2007). The
354 mafic dyke swarms and Xiong'er Group rocks possess a relatively large range of
355 initial Sr-Nd isotopic compositions (Fig. 7d), while the initial Nd isotopic



356 compositions of the diorites are relatively homogeneous (Fig. 7b). The whole-rock
357 initial Nd isotopic compositions and the zircon initial Hf isotope ratios of the Xiong'er
358 Group rocks are also enriched (Fig. 7c). The initial Pb isotopic compositions of the
359 mafic dykes and Xiong'er Group rocks are very radiogenic and variable (Fig. 8a, b),
360 which is due to the high U and Th contents of the protolith, indicating the presence of
361 an enriched subcontinental lithospheric mantle source (e.g., Hou et al., 2008; Peng et
362 al., 2004, 2007; Wang et al., 2004, 2010; Zhao et al., 2007). Based on the previous
363 discussion, the geochemical characteristics of the diorites are more compatible with a
364 crustal origin. These isotopic compositions of the diorites indicate that their sources
365 might not have been derived from the enriched mantle.

366 Additionally, the Xiong'er volcanic rocks have lower Nb/Ta ratios and Nb contents
367 (Fig. 10a). Nb and Ta share a similar valence state and atomic radii, but they can
368 undergo fractionation during the subduction process. (Jochum et al., 1986; Shannon,
369 1976). The Xiong'er volcanic rocks, with higher and positively related Ba/Th and
370 Sr/Th ratios (Fig. 10a, b), likely originated from a source influenced by early
371 subduction components, whereas the diorites appear to be less affected by early
372 subduction-related materials. Therefore, the diorites could be formed by the partial
373 melting of the mafic protolith of the lower crust on top of an enriched subcontinental
374 lithospheric mantle beneath the NCC.

375

376 **5.4 Tectonic setting**

377 Diorite is an important intermediate rock that typically forms in island arcs,
378 subduction zones, and continental collision orogenic belts along the convergent plate
379 boundaries. Oceanic island arc intermediate rocks are generally characterized by high
380 MgO, Cr, and Ni contents as boninite and low MgO, high Al₂O₃, and Na₂O/K₂O > 1



381 andesite (Hickey et al., 1982; Rapp and Watson, 1995). The continental arc
382 intermediate rocks typically show high Al_2O_3 content with a wider range of $^{87}\text{Sr}/^{86}\text{Sr}$
383 and $^{143}\text{Nd}/^{144}\text{Nd}$ isotope compositions, reflecting an obvious influence of continental
384 crust more complex and enriched source (Hawkesworth et al., 1979; Peacock et al.,
385 1994). The Paleoproterozoic diorites in the NCC lack these features of arc-related
386 rocks, meanwhile, their trace element distributions differ from those of island arc and
387 continental arc intermediate rocks. For example, these diorites do not have significant
388 enrichment in Sr, Th, and U in the primitive mantle-normalized diagram as arc-related
389 rocks (Fig. 6a). These diorites also exhibit a negative Eu anomaly in the REE diagram,
390 which is different from the arc-related rocks (Fig. 6b). The diorites in collisional
391 orogenic belts have high MgO and K_2O contents and adakite-like characteristics with
392 high Sr/Y and La/Yb ratios (Yang et al., 2015). However, Paleoproterozoic diorites in
393 the North China Craton do not show the typical arc-related element and isotopic
394 signatures, suggesting a different formation environment from subduction-related
395 magmatism.

396 Diorites can still form through crustal extension (Asmerom et al., 1990; Liu et al.,
397 2024). The North China Craton was in a post-collisional extensional environment
398 after the amalgamation (Zhai, 2010), where the magmatic genesis became more
399 complex (Bonin, 2004). Zircon is relatively stable and may record more information,
400 therefore, its trace elements offer significant potential for distinguishing between
401 different tectonic environments. Zircon samples with La contents less than 1 ppm
402 were selected for discussion to ensure accurate information from zircon trace element
403 contents without interference from the inclusion of other accessory phases (Zou et al.,
404 2019). All zircons from the diorites plot within the continental area in the U/Yb versus
405 Y diagram (Fig. 11a), and most of them tend to fall into a rift-controlled tectonic



406 environment in the zircon tectonic discrimination diagrams (Fig. 11b, c; Carly et al.,
407 2014).

408 Furthermore, high-field strength elements, such as Zr, Nb, Ta, Hf, and Th, are
409 important in tectonic discrimination diagrams. The distinctive Th content in arc
410 magmas is primarily due to its low solubility in subduction zone fluids and its
411 contribution from sedimentary components (e.g., Bailey and Ragnasdottir, 1994;
412 Pearce and Peate, 1995). The arc-related/orogenic magmas usually have less Nb than
413 those in within-plate settings (e.g., Pearce and Peate, 1995; Sun and McDonough,
414 1989). Nb in zircon is thought to be incorporated through xenotime-type substitution
415 (Schulz et al., 2006) and is suggested to reflect the magma composition with minimal
416 influence from magmatic fractionation (Hoskin et al., 2000; Schulz et al., 2006). In
417 the Nb/Hf versus Th/U and Hf/Th versus Th/Nb diagrams, zircons from the Fudian
418 and Gushicun diorites plot both within the arc-related/orogenic area and near this area
419 (Fig. 11d, e). The Jiuganshan and Muzhijie diorites plot both in the
420 arc-related/orogenic and within-plate/anorogenic areas (Fig. 11d, e). The whole-rock
421 Ta/Yb and Th/Yb ratios of these diorites are uniform (Fig. 11f), all falling within the
422 overlapping area of the ACM (active continental margins) and WPVZ (Within-Plate
423 Volcanic Zone). These may indicate that the post-collisional extension during this
424 period may ultimately lead to rift evolution continuously and progressively. The
425 diorites preserve a record of the superimposition of representative components from
426 multiple tectonic settings.

427 After the 1.85 Ga collisional event, the North China Craton entered a prolonged
428 post-collisional extensional stage. The magmatism was primarily controlled by crustal
429 remelting, leading to the widespread formation of various crust-derived granites in the
430 orogenic belts at the end of the Paleoproterozoic (Deng et al., 2016; Wang et al.,



431 [2023b; Xu et al., 2024](#)). However, after 1.78 Ga, the crust-derived diorites show
432 transitional features in their tectonic setting, retaining some remnant effects of the
433 orogenic magmatism while gradually evolving toward intraplate magmatism. It
434 reflects the ongoing extension of the North China Craton after its amalgamation.

435

436 **6 Conclusions**

437 The Jiguanshan diorite yields a zircon U-Pb age of about 1.78 Ga. It displays
438 geochemical features in common with other diorite intrusions within the NCC. The
439 diorite intrusion was contemporaneous with the Xiong'er volcanic rocks and the mafic
440 dyke swarms, representing a significant period of magmatism.

441 The late Paleoproterozoic diorites primarily resulted from the partial melting of the
442 mafic protolith. The Sr-Nd-Pb-Hf isotopic characteristics indicate that the source was
443 not the same as that for the Xiong'er volcanic rocks or mafic dyke swarms. Instead,
444 they are more likely derived from the lower crust of the NCC.

445 The formation of Paleoproterozoic diorites in the North China Craton is unlikely to be
446 arc-related. Instead, it is associated with a rift setting. The formation of diorite records
447 the transition of crustal origin rocks from orogenic-related magmatism to intraplate
448 magmatism during the post-collision extensional stage. It reflects the ongoing
449 extension of the North China Craton after its amalgamation.

450

451 **Acknowledgements**

452 This study was financially supported by the Strategic Priority Research Program of
453 the Chinese Academy of Sciences (grant Nos. XDA0430203) and the National
454 Natural Science Foundation of China (grant Nos. 42202069 and 41872049). Zhiyi



455 Wang was financially supported by China Scholarship Council (202306340065). We

456 thank P. Xiao and Z.-H. Hou for assistance with the analysis.

457

458 **Author contributions:**

459 Zhiyi Wang: Investigation, Writing - Review & Editing;

460 Shuhao Tang, Yiru Ji, Jianfeng He: Investigation, Review & Editing;

461 Wolfgang Siebel.: Conceptualization, Writing - Review & Editing;

462 Jun He & Fukun Chen: Supervision, Writing - Review & Editing, Funding acquisition.

463

464 **Competing interests:**

465 The authors declare no competing financial and non-financial interests for this study.

466

467



References

- Asmerom, Y., Snow, J. K., Holm, D. K., Jacobsen, S. B., Wernicke, B. P., and Lux, D. R.: Rapid uplift and crustal growth in extensional environments: An isotopic study from the Death Valley region, California. *Geology*, 18, 223–226. [https://doi.org/10.1130/0091-7613\(1990\)018<0223:RUACGI>2.3.CO;2](https://doi.org/10.1130/0091-7613(1990)018<0223:RUACGI>2.3.CO;2), 1990.
- Bailey, E.H., and Ragnarsdottir, K.V.: Uranium and thorium solubilities in subduction zone fluids. *Earth Planet. Sci. Lett.*, 124, 119–129. [https://doi.org/10.1016/0012-821X\(94\)00071-9](https://doi.org/10.1016/0012-821X(94)00071-9), 1994.
- Beard, J.S., and Lofgren, G.E.: Dehydration melting and water-saturated melting of basaltic and andesitic greenstones and amphibolites at 1, 3, and 6.9 kb. *J. Petrol.* 32, 365–401. <https://doi.org/10.1093/petrology/32.2.365>, 1991.
- BGMRH (Bureau of Geology and Mineral Resources of Henan Province): Geological map of the Henan Province. Sheet I-49-(23) (Lushan) scale 1:200,000 (in Chinese), 1994.
- Bonin, B.: Do coeval mafic and felsic magmas in post-collisional to within-plate regimes necessarily imply two contrasting, mantle and crustal sources? A review. *Lithos*, 78, 1–24. <https://doi.org/10.1016/j.lithos.2004.04.042>, 2004.
- Carley, T.L., Miller, C.F., Wooden, J.L., Padilla, A.J., Schmitt, A.K., Economos, R.C., Bindeman, I.N., and Jordan, B.T.: Iceland is not a magmatic analog for the Hadean: evidence from the zircon record. *Earth Planet. Sci. Lett.*, 405, 85–97. <https://doi.org/10.1016/j.epsl.2014.08.015>, 2014.
- Castillo, P., Janney, P., and Solidum, R.: Petrology and geochemistry of Camiguin Island, southern Philippines: insights to the source of adakites and other lavas in a complex arc setting. *Contrib. Mineral. Petrol.*, 134, 33–51. <https://doi.org/10.1007/s004100050467>, 1999.
- Chen, F., Hegner, E., and Todt, W.: Zircon ages, Nd isotopic and chemical compositions of orthogneisses from the Black Forest, Germany - evidence for a Cambrian magmatic arc. *Int. J. Earth Sci.*, 88, 791–802. <https://doi.org/10.1007/s005310050306>, 2000.
- Chen, F., Li, X. H., Wang, X. L., Li, Q. L., and Siebel, W.: Zircon age and Nd-Hf isotopic composition of the Yunnan Tethyan belt, southwestern China. *Int. J. Earth Sci.*, 96, 1179–1194. <https://doi.org/10.1007/s00531-006-0146-y>, 2007.
- Chen, L., Zheng, Y.F., Xu, Z., and Zhao, Z.F.: Generation of andesite through partial melting of basaltic metasomatites in the mantle wedge: Insight from quantitative study of Andean andesites. *Geosci. Front.*, 12, 101124. <https://doi.org/10.1016/j.gsf.2020.12.005>, 2021.
- Cui, M.L., Zhang, B.L., Peng, P., Zhang, L.C., Shen, X.L., Guo, Z.H., and Huang, X.F.: Zircon/baddeleyite U-Pb dating for the Paleoproterozoic intermediate-acid intrusive rocks in Xiaoshan Mountains, west of Henan Province and their constraints on the age of the Xiong'er Volcanic Province. *Acta Petrol. Sin.* (in Chinese with English abstract), 26, 1541–1549, 2010.



- 502 Cui, M.L., Zhang, B.L., and Zhang, L.C.: U–Pb dating of baddeleyite and zircon from the Shizhaigou
503 diorite in the southern margin of North China Craton: Constraints on the timing and tectonic setting
504 of the Paleoproterozoic Xiong'er group. *Gondwana Res.*, 20, 184–193.
505 <https://doi.org/10.1016/j.gr.2011.01.010>, 2011.
- 506 Defant, M., and Drummond, M.: Derivation of some modern arc magmas by melting of young
507 subducted lithosphere. *Nature*, 347, 662–665. <https://doi.org/10.1038/347662a0>, 1990.
- 508 Deng, X. Q., Peng, T. P., and Zhao, T. P.: Geochronology and Geochemistry of the Late
509 Paleoproterozoic Aluminous A-Type Granite in the Xiaoqinling Area along the Southern Margin of
510 the North China Craton: Petrogenesis and Tectonic Implications. *Precambrian Res.*, 285: 127–146.
511 <https://doi.org/10.1016/j.precamres.2016.09.013>, 2016.
- 512 Diwu, C.R., Liu, X., and Sun, Y.: The composition and evolution of the Taihua Complex in the southern
513 North China Craton. *Acta Petrol. Sin.* (in Chinese with English abstract), 34, 999–1018, 2018.
- 514 Diwu, C.R., Sun, Y., Zhao, Y., and Lai, S.C.: Early Paleoproterozoic (2.45–2.20 Ga) magmatic activity
515 during the period of global magmatic shutdown: Implications for the crustal evolution of the
516 southern North China Craton. *Precambrian Res.*, 255, 627–640.
517 <https://doi.org/10.1016/j.precamres.2014.08.001>, 2014.
- 518 Gao, J.F., Zhou, M.F., Robinson, P.T., Wang, C.Y., Zhao, J.H., and Malpas, J.: Magma mixing recorded
519 by Sr isotopes of plagioclase from dacites of the Quaternary Tengchong volcanic field, SE Tibetan
520 Plateau. *J. Asian Earth Sci.*, 98, 1–17. <https://doi.org/10.1016/j.jseas.2014.10.036>, 2015.
- 521 Geng, Y.S., Du, L.L., and Ren, L.D.: Growth and reworking of the early Precambrian continental crust
522 in the North China Craton: Constraints from zircon Hf isotopes. *Gondwana Res.*, 21, 517–529.
523 <https://doi.org/10.1016/j.gr.2011.07.006>, 2012.
- 524 Gorton, M.P., and Schandl, E.S.: From continents to island arcs: A geochemical index of tectonic
525 setting for arc-related and within-plate felsic to intermediate volcanic rocks. *Can. Mineral.*, 38,
526 1065–1073. <https://doi.org/10.2113/gscanmin.38.5.1065>, 2000.
- 527 Grimes, C.B., John, B.E., Kelemen, P.B., Mazdab, F., Wooden, J.L., Cheadle, M.J., Hanghøj, K., and
528 Schwartz, J.J.: Trace element chemistry of zircons from oceanic crust: a method for distinguishing
529 detrital zircon provenance. *Geology*, 35, 643–646. <https://doi.org/10.1130/G23603A.1>, 2007.
- 530 Hawkesworth, C.J., Norry, M.J., Roddick, J.C., Baker, P.E., Francis, P.W., and Thorpe, R.S.:
531 $^{143}\text{Nd}/^{144}\text{Nd}$, $^{87}\text{Sr}/^{86}\text{Sr}$, and incompatible element variations in calc-alkaline andesites and
532 plateau lavas from South America. *Earth Planet. Sci. Lett.*, 42, 45–57.
533 [https://doi.org/10.1016/0012-821X\(79\)90189-4](https://doi.org/10.1016/0012-821X(79)90189-4), 1979.
- 534 Hawkesworth, C.J., and Kemp, A.I.S.: Using hafnium and oxygen isotopes in zircons to unravel the
535 record of crustal evolution. *Chem. Geol.*, 226, 144–162.
536 <https://doi.org/10.1016/j.chemgeo.2005.09.018>, 2006.



- 537 He, J., Qi, Y., Fan, X., and Chen, F.: Petrogenesis of the Taishanmiao A-type granite in the eastern
538 Qinling orogenic belt: Implications for tectonic transition and mineralization in the Late Cretaceous.
539 *J. Geol.*, 129, 97-114. <https://doi.org/10.1086/713726>, 2021.
- 540 He, Y.H., Zhao, G.C., Sun, M., and Wilde, S.A.: Geochemistry, isotope systematics and petrogenesis of
541 the volcanic rocks in the Zhongtiao Mountain: An alternative interpretation for the evolution of the
542 southern margin of the North China Craton. *Lithos*, 102, 158-178.
543 <https://doi.org/10.1016/j.lithos.2007.09.004>, 2008.
- 544 He, Y.H., Zhao, G.C., Sun, M., and Xia, X.: SHRIMP and LA-ICP-MS zircon geochronology of the
545 Xiong'er volcanic rocks: Implications for the Paleo-Mesoproterozoic evolution of the southern
546 margin of the North China Craton. *Precambrian Res.*, 168, 213-222.
547 <https://doi.org/10.1016/j.precamres.2008.09.011>, 2009.
- 548 He, Y.H., Zhao, G.C., Sun, M., and Han, Y.G.: Petrogenesis and tectonic setting of volcanic rocks in the
549 Xiaoshan and Waifangshan areas along the southern margin of the North China Craton: Constraints
550 from bulk-rock geochemistry and Sr–Nd isotopic composition. *Lithos*, 114, 186-199.
551 <https://doi.org/10.1016/j.lithos.2009.08.008>, 2010.
- 552 Hickey, R.L., and Frey, F.A.: Geochemical characteristics of boninite series volcanics: implications for
553 their source. *Geochim. Cosmochim. Acta*, 46(11), 2099–2115.
554 [https://doi.org/10.1016/0016-7037\(82\)90188-0](https://doi.org/10.1016/0016-7037(82)90188-0), 1982.
- 555 Hou, G.T., Li, J.H., Yang, M.H., Yao, W.H., Wang, C.C., and Wang, Y.X.: Geochemical constraints on
556 the tectonic environment of the Late Paleoproterozoic mafic dyke swarms in the North China
557 Craton. *Gondwana Res.*, 13, 103-116. <https://doi.org/10.1016/j.gr.2007.06.005>, 2008.
- 558 Hoskin, P.W.O., Kinny, P.D., Wyborn, D., and Chappell, B.W.: Identifying accessory mineral saturation
559 during differentiation in granitoid magmas: an integrated approach. *J. Petrol.*, 41, 1365–1396.
560 <https://doi.org/10.1093/petrology/41.9.1365>, 2000.
- 561 Hu, G.Y., Zeng, L.S., Gao, L.E., Liu, Q.P., Chen, H., and Guo, Y.S.: Diverse magma sources for the
562 Himalayan leucogranites: Evidence from B–Sr–Nd isotopes. *Lithos*, 314-315, 88-99.
563 <https://doi.org/10.1016/j.lithos.2018.05.022>, 2018.
- 564 Huang, X.L., Xu, Y.G., and Liu, D.Y.: Geochronology, petrology and geochemistry of the granulite
565 xenoliths from Nushan, east China: implication for a heterogeneous lower crust beneath the
566 Sino-Korean Craton. *Geochim. Cosmochim. Acta*, 68, 127-149.
567 [https://doi.org/10.1016/S0016-7037\(03\)00416-2](https://doi.org/10.1016/S0016-7037(03)00416-2), 2004.
- 568 Jackson, M.D., Cheadle, M.J., and Atherton, M.P.: Quantitative modeling of granitic melt generation
569 and segregation in the continental crust. *J. Geophys. Res. Solid Earth*, 108, 2332.
570 <https://doi.org/10.1029/2001JB001050>, 2003.
- 571 Jochum, K.P., Seufert, H.M., Spettel, B., and Palme, H.: The solar-system abundances of Nb, Ta, and Y,
572 and the relative abundances of refractory lithophile elements in differentiated planetary bodies.
573 *Geochim. Cosmochim. Acta*, 50, 1173-1183. [https://doi.org/10.1016/0016-7037\(86\)90400-X](https://doi.org/10.1016/0016-7037(86)90400-X), 1986.



- 574 Kelemen, P.B.: Genesis of high Mg[#] andesites and the continental crust. *Contrib. Mineral. Petrol.*, 120,
575 1-19. <https://doi.org/10.1007/BF00311004>, 1995.
- 576 Le Bas, M.J., Le Maitre, R.W., Streckeisen, A., and Zanettin, B.: A Chemical Classification of
577 Volcanic-Rocks Based on the Total Alkali Silica Diagram. *J. Petrol.*, 27, 745-750.
578 <https://doi.org/10.1093/petrology/27.3.745>, 1986.
- 579 Liu, A.L., Hai, L.F., Liu, J.K., Zhang X.J., Li H.F., Zhao F.S., Zhao G.L., and Bai J.H.: Geochronology,
580 Geochemistry, and Sr-Nd-Hf Isotopes of the Diorite Porphyrites from the Weining Beishan Area,
581 Ningxia Hui Autonomous Region: Constraints on Their Source and Tectonic Implications. *J. Earth*
582 *Sci.* 35, 462–475. <https://doi.org/10.1007/s12583-021-1491-2>, 2024.
- 583 Liu, D.Y., Nutman, A.P., Compston, W., Wu, J.S., and Shen, Q.H.: Remnants of ≥ 3800 Ma crust in the
584 Chinese part of the Sino-Korean Craton. *Geology*, 20, 339-342.
585 [https://doi.org/10.1130/0091-7613\(1992\)020<0339:ROMCIT>2.3.CO;2](https://doi.org/10.1130/0091-7613(1992)020<0339:ROMCIT>2.3.CO;2), 1992.
- 586 Liu, Y.S., Hu, Z.C., Zong, K.Q., Gao, C.G., Gao, S., Xu, J.A., and Chen, H.H.: Reappraisal and
587 refinement of zircon U-Pb isotope and trace element analyses by LA-ICP-MS. *Chin. Sci. Bull.* (in
588 Chinese with English abstract), 1535-1546, 2010.
- 589 Ma, J.F., Qu, C.H., Zhou, Y.Y., and Zhao, T.P.: The genesis of ca. 1.78 Ga granitoids in the Xiong'er
590 large igneous province: Implications for continental crust generation. *Geol. Soc. Am. Bull.*, 135,
591 3213-3227. <https://doi.org/10.1130/B36694.1>, 2023a.
- 592 Ma, J.F., Wang, X.L., Yang, A.Y., and Zhao, T.P.: Tracking crystal-melt segregation and accumulation
593 in the intermediate magma reservoir. *Geophys. Res. Lett.*, 50, e2022GL102540.
594 <https://doi.org/10.1029/2022GL102540>, 2023b.
- 595 Maniar, P.D., and Piccoli, P.M.: Tectonic discrimination of granitoids. *Geol. Soc. Am. Bull.*, 101,
596 635-643. [https://doi.org/10.1130/0016-7606\(1989\)101<0635:TDOG>2.3.CO;2](https://doi.org/10.1130/0016-7606(1989)101<0635:TDOG>2.3.CO;2), 1989.
- 597 Pan, Z.J., Zhang, Q., Chen, G., Jiao, S.T., Du, X.L., Miao, X.Q., Wang, J.R., and An, Y.: Relation
598 between Mesozoic magmatism and plate subduction in eastern China: Comparison among
599 Zhejiang-Fujian, Japan arc and Andes arc. *Acta Petrol. Sin.* (in Chinese with English abstract), 33,
600 1507–1523, 2017.
- 601 Peacock, S.M., Rushmer, T., and Thompson, A.B.: Partial melting of subducting oceanic crust. *Earth*
602 *Planet. Sci. Lett.*, 121, 227-244. [https://doi.org/10.1016/0012-821X\(94\)90042-6](https://doi.org/10.1016/0012-821X(94)90042-6), 1994.
- 603 Pearce, J.A.: Role of the sub-continental lithosphere in magma genesis at active continental margins.
604 In: Hawkesworth, C.J., Norry, M.J. (Eds.): *Continental Basalts and Mantle Xenoliths*. Shiva
605 Publishing Ltd., Nantwich, 230–249. ISBN: 978-0906812341, 1983.
- 606 Pearce, J.A., and Peate, D.W.: Tectonic implications of the composition of volcanic arc magmas. *Annu.*
607 *Rev. Earth Planet. Sci.*, 23, 251–285. <https://doi.org/10.1146/annurev.ea.23.050195.001343>, 1995.



- 608 Peccerillo, A., and Taylor, S.R.: Geochemistry of Eocene calcalkaline volcanic rocks from the
609 Kastamonu area, northern Turkey. *Contrib. Mineral. Petrol.*, 58, 130–143.
610 <https://doi.org/10.1007/BF00384745>, 1976.
- 611 Peng, P., Zhai, M.G., Zhang, H.F., Zhao, T.P., and Ni, Z.Y.: Geochemistry and geological significance
612 of the 1.8 Ga mafic dyke swarms in the North China Craton: an example from the juncture of
613 Shanxi, Hebei and Inner Mongolia. *Acta Petrol. Sin.* (in Chinese with English abstract), 20,
614 439–456, 2004.
- 615 Peng, P., Zhai, M.G., Guo, J.H., Kusky, T., and Zhao, T.P.: Nature of mantle source contributions and
616 crystal differentiation in the petrogenesis of the 1.78 Ga mafic dykes in the central North China
617 craton. *Gondwana Res.*, 12, 29–46. <https://doi.org/10.1016/j.gr.2006.10.022>, 2007.
- 618 Peng, P., Zhai, M.G., Ernst, R.E., Guo, J.H., Liu, F., and Hu, B.: A 1.78 Ga large igneous province in
619 the North China craton: The Xiong'er Volcanic Province and the North China dyke swarm. *Lithos*,
620 101, 260–280. <https://doi.org/10.1016/j.lithos.2007.07.006>, 2008.
- 621 Petford, N., and Atherton, M.: Na-rich partial melts from newly underplated basaltic crust: the
622 Cordillera Blanca Batholith, Peru. *J. Petrol.*, 37, 1491–1521.
623 <https://doi.org/10.1093/petrology/37.6.1491>, 1996.
- 624 Rapp, R.P., and Watson, E.B.: Dehydration melting of metabasalt at 8–32 kbar: Implications for
625 continental growth and crust-mantle recycling. *J. Petrol.*, 36, 891–931.
626 <https://doi.org/10.1093/petrology/36.4.891>, 1995.
- 627 Reubi, O., and Blundy, J.: A dearth of intermediate melts at subduction zone volcanoes and the
628 petrogenesis of arc andesites. *Nature*, 461, 1269–1273. <https://doi.org/10.1038/nature08510>, 2009.
- 629 Roberts, M.P., and Clemens, J.D.: Origin of high-potassium, calc-alkaline, I-type granitoids. *Geology*,
630 21, 825–828. [https://doi.org/10.1130/0091-7613\(1993\)021<0825:OOHPTA>2.3.CO;2](https://doi.org/10.1130/0091-7613(1993)021<0825:OOHPTA>2.3.CO;2), 1993.
- 631 Schulz, B., Klemm, R., and Brätz, H.: Host rock compositional controls on zircon trace element
632 signatures in metabasites from the Austroalpine basement. *Geochim. Cosmochim. Acta*, 70, 697–
633 710. <https://doi.org/10.1016/j.gca.2005.10.001>, 2006.
- 634 Shannon, R.D.: Revised effective ionic-radii and systematic studies of interatomic distances in halides
635 and chalcogenides. *Acta Crystallogr. A*, 32, 751–767. <https://doi.org/10.1107/S0567739476001551>,
636 1976.
- 637 Siebel, W., Reitter, E., Wenzel, T., and Blaha U.: Sr isotope systematics of K-feldspars in plutonic rocks
638 revealed by the Rb–Sr microdrilling technique. *Chem. Geol.*, 222, 183–199.
639 <https://doi.org/10.1016/j.chemgeo.2005.06.012>, 2005.
- 640 Stern, C., and Kilian, R.: Role of the subducted slab, mantle wedge and continental crust in the
641 generation of adakites from the Andean Austral Volcanic Zone. *Contrib. Mineral. Petrol.*, 123,
642 263–281. <https://doi.org/10.1007/s004100050155>, 1996.



- 643 Streck, M.J., Leeman, W.P., and Chesley, J.: High-magnesian andesite from Mount Shasta: A product of
644 magma mixing and contamination, not a primitive mantle melt. *Geology*, 35, 351-354.
645 <https://doi.org/10.1130/G23286A.1>, 2007.
- 646 Sun, S.S., and McDonough, W.F.: Chemical and isotopic systematics of oceanic basalts: implications
647 for mantle composition and processes. *Geol. Soc. London, Spec. Publ.*, 42, 313-345.
648 <https://doi.org/10.1144/GSL.SP.1989.042.01.19>, 1989.
- 649 Vermeesch, P.: IsoplotR: A free and open toolbox for geochronology. *Geoscience Frontiers*, 9,
650 1479-1493. <https://doi.org/10.1016/j.gsf.2018.04.001>, 2018.
- 651 Wang, C.M., Lu, Y.J., He, X.Y., Wang, Q.H., and Zhang, J.: The Paleoproterozoic diorite dykes in the
652 southern margin of the North China Craton: Insight into rift-related magmatism. *Precambrian Res.*,
653 277, 26-46. <https://doi.org/10.1016/j.precamres.2016.02.009>, 2016.
- 654 Wang, J.L., Zhang, H.F., Zhang, J., Santosh, M., and Bao, Z. A.: Highly heterogeneous Pb isotope
655 composition in the Archean continental lower crust: Insights from the high-grade metamorphic suite
656 of the Taihua Group, Southern North China Craton. *Precambrian Res.*, 350, 105927.
657 <https://doi.org/10.1016/j.precamres.2020.105927>, 2020.
- 658 Wang, X., Huang X., and Yang F.: Revisiting the Lushan-Taihua Complex: New perspectives on the
659 Late Mesoproterozoic-Early Neoproterozoic crustal evolution of the southern North China Craton:
660 *Precambrian Res.*, 325, 132–149. <https://doi.org/10.1016/j.precamres.2019.02.020>, 2019.
- 661 Wang, X.L., Jiang, S.Y., and Dai, B.Z.: Melting of enriched Archean subcontinental lithospheric
662 mantle: Evidence from the ca. 1760 Ma volcanic rocks of the Xiong'er Group, southern margin of
663 the North China Craton. *Precambrian Res.*, 182, 204–216.
664 <https://doi.org/10.1016/j.precamres.2010.08.007>, 2010.
- 665 Wang, Y.J., Fan, W.M., Zhang, Y., Guo, F., Zhang, H., and Peng, T.: Geochemical, $^{40}\text{Ar}/^{39}\text{Ar}$
666 geochronological and Sr-Nd isotopic constraints on the origin of Paleoproterozoic mafic dikes from
667 the southern Taihang Mountains and implications for the ca. 1800 Ma event of the North China
668 Craton. *Precambrian Res.*, 135, 55-77. <https://doi.org/10.1016/j.precamres.2004.07.005>, 2004.
- 669 Wang, Z.Y., Cheng, H., Zhao, J.X., Ye R.S., Li W.Y., He J.F., and Chen F.K.: Sr-Nd-Pb isotopic
670 composition of the Chinese national standard igneous rock powders measured by thermal ionization
671 mass spectrometry. *Geol. J. China Univ.* (in Chinese with English abstract), 29, 679-692, 2023a.
- 672 Wang, M.X., Wang Z.Y., Zhao J.X., Qi Z.Q., He J., and Chen F.K.: Petrogenesis and Geologic
673 Implication of the Late Paleoproterozoic A-type Xiaohe Pluton along the Southern Margin of the
674 North China Craton. *Geol. J. China Univ.* (in Chinese with English abstract), 29(6): 809-830,
675 2023b.
- 676 Wolf, M.B., and Wyllie, P.J.: Garnet growth during amphibolite anatexis: Implications of a
677 garnetiferous restite. *J. Geol.*, 101, 357-373. <https://doi.org/10.1086/648229>, 1993.



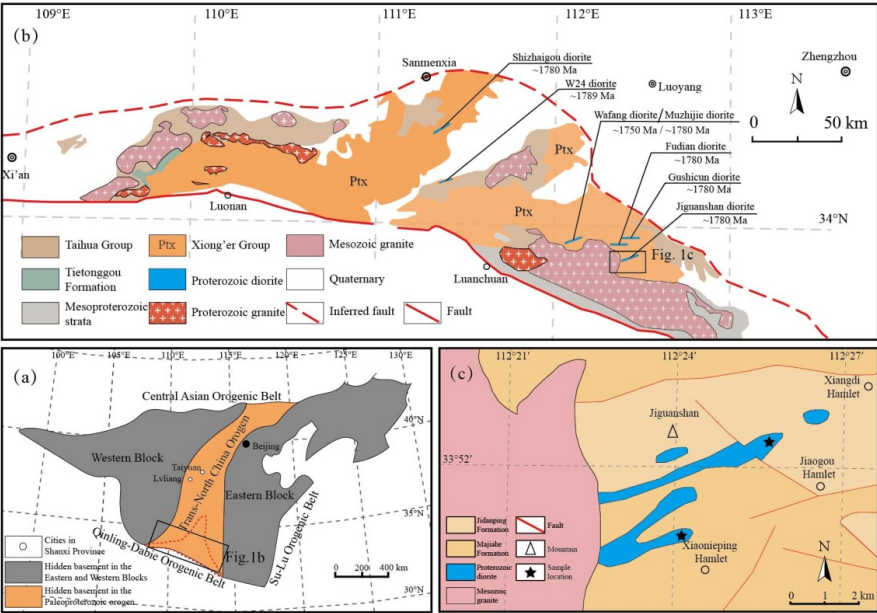
- 678 Wolf, M., Romer, R.L., and Glodny, J.: Isotope disequilibrium during partial melting of
679 metasedimentary rocks. *Geochim. Cosmochim. Acta* 257, 163-183.
680 <https://doi.org/10.1016/j.gca.2019.05.008>, 2019.
- 681 Xu, J.H., Jiang, Y.P., Hu, S.L., Zhang Z.W., Wu C.Q., Zheng C.F., Li X.Y., Jin Z.R., Zhang S.S., and
682 Zhou Y.T.: Petrogenesis and Tectonic Implications of the Paleoproterozoic A-Type Granites in the
683 Xiong'er shan Area along the Southern Margin of the North China Craton. *J. Earth Sci.*, 35, 416–
684 429. <https://doi.org/10.1007/s12583-021-1424-0>, 2024.
- 685 Yang, J.H., Cawood, P.A., Du, Y.S., Huang, H., Huang, H.W., and Tao, P.: Large Igneous Province and
686 magmatic arc sourced Permian–Triassic volcanogenic sediments in China. *Sedimentary Geol.*
687 261-262, 120-131. <https://doi.org/10.1016/j.sedgeo.2012.03.018>, 2012.
- 688 Yang, Z.M., Lu, Y.J., Hou, Z.Q., and Chang, Z.S.: High-Mg diorite from Qulong in southern Tibet:
689 implications for the genesis of adakite-like intrusions and associated porphyry Cu deposits in
690 collisional orogens. *J. Petrol.*, 56, 227–254. <https://doi.org/10.1093/petrology/egu076>, 2015.
- 691 Zeng, L.S., Asimow, P.D., and Saleeby, J.B.: Coupling of anatectic reactions and dissolution of
692 accessory phases and the Sr and Nd isotope systematics of anatectic melts from a metasedimentary
693 source. *Geochim. Cosmochim. Acta*, 69, 3671-3682. <https://doi.org/10.1016/j.gca.2005.02.035>,
694 2005.
- 695 Zhai, M.G.: Tectonic evolution and metallogenesis of North China Craton. *Mineral Deposits* (in
696 Chinese with English abstract), 29, 24-36, 2010.
- 697 Zhao, G.C., Cawood, P.A., Wilde, S.A., Min, S., and Lu, L.Z.: Metamorphism of basement rocks in the
698 Central Zone of the North China Craton: implications for Paleoproterozoic tectonic evolution.
699 *Precambrian Res.*, 103, 55-88. [https://doi.org/10.1016/S0301-9268\(00\)00076-0](https://doi.org/10.1016/S0301-9268(00)00076-0), 2000a.
- 700 Zhao, G.C., He, Y.H., and Sun, M.: Xiong'er volcanic belt at the North China Craton: The Xiong'er
701 volcanic belt at the southern margin of the North China Craton: Petrographic and geochemical
702 evidence for its outboard position in the Paleo-Mesoproterozoic Columbia Supercontinent.
703 *Gondwana Res.*, 16, 170–181. <https://doi.org/10.1016/j.gr.2009.02.004>, 2009.
- 704 Zhao, G.C., Wilde, S.A., Cawood, P.A., and Lu, L.Z.: Petrology and P-T path of the Fuping mafic
705 granulites: implications for tectonic evolution of the central zone of the North China Craton. *J.*
706 *Metamorphic Geol.*, 18, 375-391. <https://doi.org/10.1046/j.1525-1314.2000.00264.x>, 2000b.
- 707 Zhao, G.C., Wilde, S.A., Cawood, P.A., and Sun, M.: Archean blocks and their boundaries in the North
708 China Craton: lithological, geochemical, structural and P–T path constraints and tectonic evolution.
709 *Precambrian Res.* 107, 45-73. [https://doi.org/10.1016/S0301-9268\(00\)00154-6](https://doi.org/10.1016/S0301-9268(00)00154-6), 2001.
- 710 Zhao, G.C., and Zhai, M.G.: Lithotectonic elements of Precambrian basement in the North China
711 Craton: Review and tectonic implications. *Gondwana Res.*, 23, 1207-1240.
712 <https://doi.org/10.1016/j.gr.2012.08.016>, 2013.



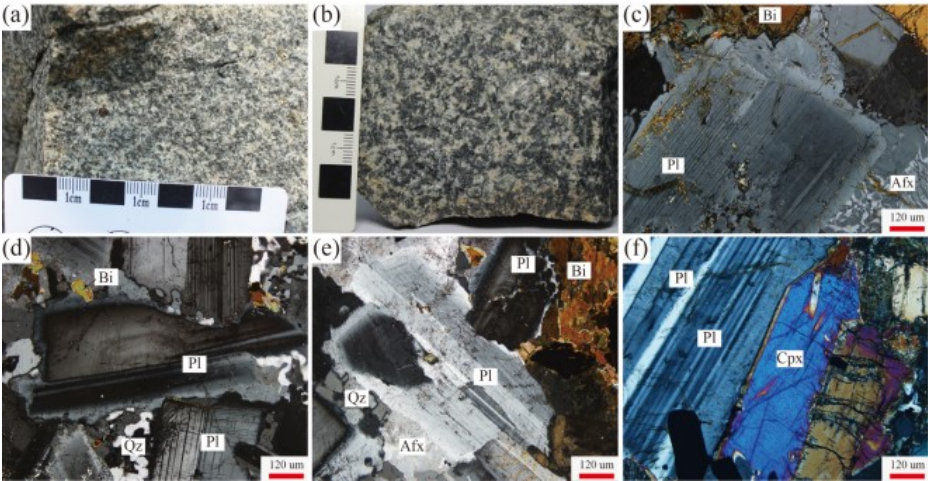
- 713 Zhao, T.P.: The characteristic and genesis of Proterozoic potassic volcanic rock in southern margin of
714 the North plate. Doctoral dissertation, Institute of Geology and Geophysics, Chinese Academy of
715 Sciences, Beijing, 102p, 2000.
- 716 Zhao, T.P., Xu, Y.H., and Zhai, M.G.: Petrogenesis and tectonic setting of the Paleoproterozoic
717 Xiong'er Group in the southern part of the North China Craton: A review. *Geol. J. China Univ.* (in
718 Chinese with English abstract), 13, 191–206, 2007.
- 719 Zhao, T.P., Zhou, M.F., Zhai, M.G., and Xia, B.: Paleoproterozoic rift-related volcanism of the Xiong'er
720 Group, North China Craton: Implications for the breakup of Columbia. *Int. Geol. Rev.*, 44, 336–351.
721 <https://doi.org/10.2747/0020-6814.44.4.336>, 2002
- 722 Zhao, T.P., Zhai, M.G., Xia, B., Li, H.M., and Zhang, Y.X.: Zircon U-Pb SHRIMP dating for the
723 volcanic rocks of the Xiong'er Group: Constraints on the initial formation age of the cover of the
724 North China Craton. *Chin. Sci. Bull.* (in Chinese with English abstract), 49, 2495–2502, 2004.
- 725 Zou, X.Y., Qin, K.Z., Han, X.L., Li, G.M., Evans, N.J., Li, Z.Z., and Yang, W.: Insight into zircon REE
726 oxy-barometers: A lattice strain model perspective. *Earth Planet. Sci. Lett.*, 506, 87–96.
727 <https://doi.org/10.1016/j.epsl.2018.10.031>, 2019.
- 728



729 **Figures**



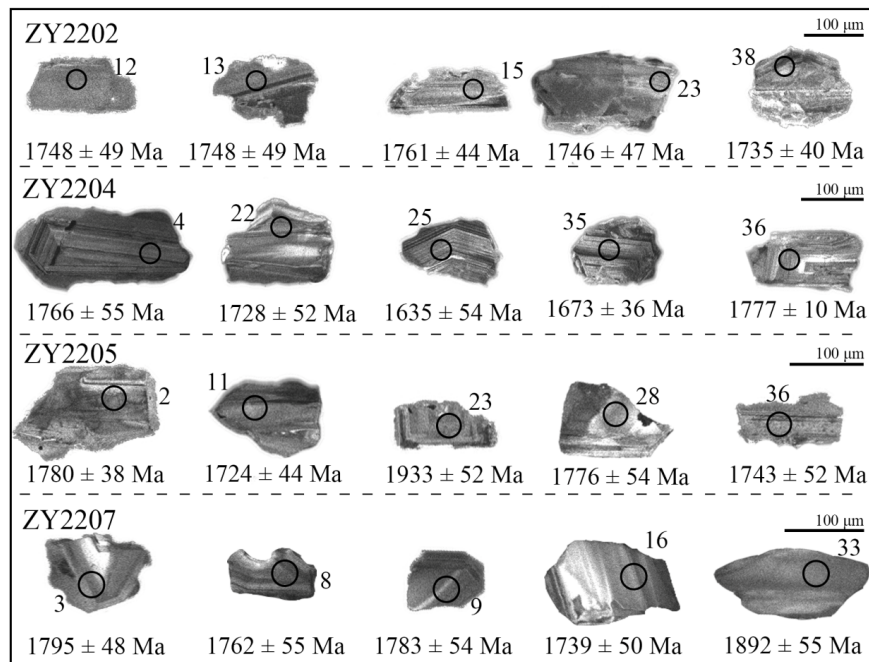
730
731 **Figure 1** (a) Tectonic sketch of the North China Craton (after Zhao et al., 2001); (b) Geological map of
732 the southern margin of the North China Craton (after Diwu et al., 2014; diorites from Cui et al.,
733 2011; Ma et al 2023a, b; Wang et al., 2016; Zhao et al., 2004); (c) Geological map of the Jiguanshan
734 diorite (after BGMRH, 1994)



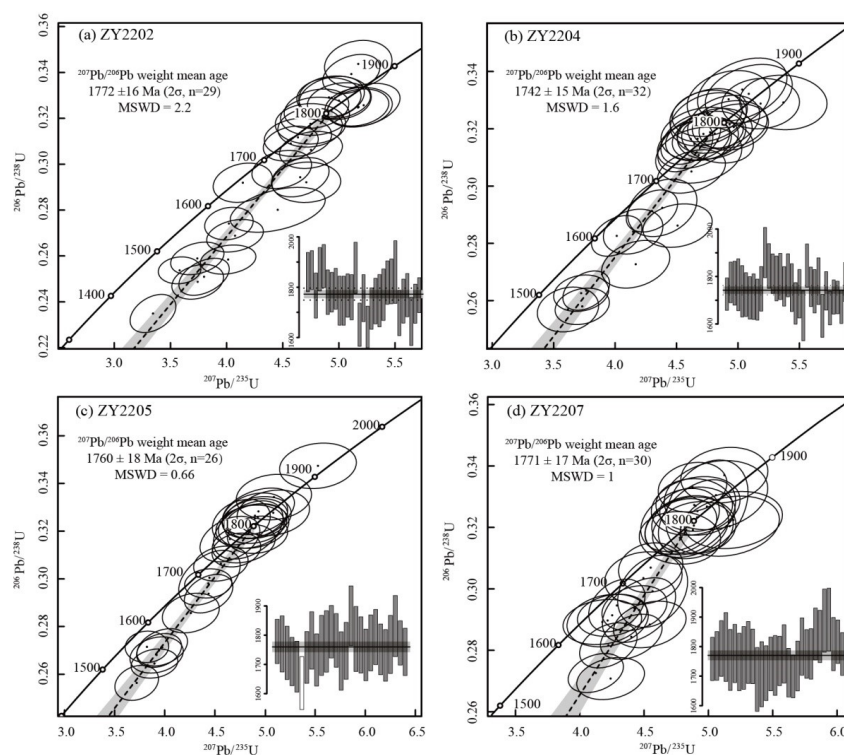
737



738 **Figure 2** (a-b) Field photographs and representative hand specimens of the Jiguanshan diorite; (c-f)
739 Micrographs under the plane-polarized light of the Jiguanshan diorite. Mineral abbreviations: Afs,
740 alkali feldspar; Bi, biotite; Cpx, Clinopyroxene; Pl, plagioclase; Qz, quartz



741
742 **Figure 3** Cathodoluminescence (CL) images of representative zircon grains from the Jiguanshan
743 diorite



744

745 **Figure 4** (a-d) Zircon U–Pb concordia diagrams of the Jiguanshan diorite

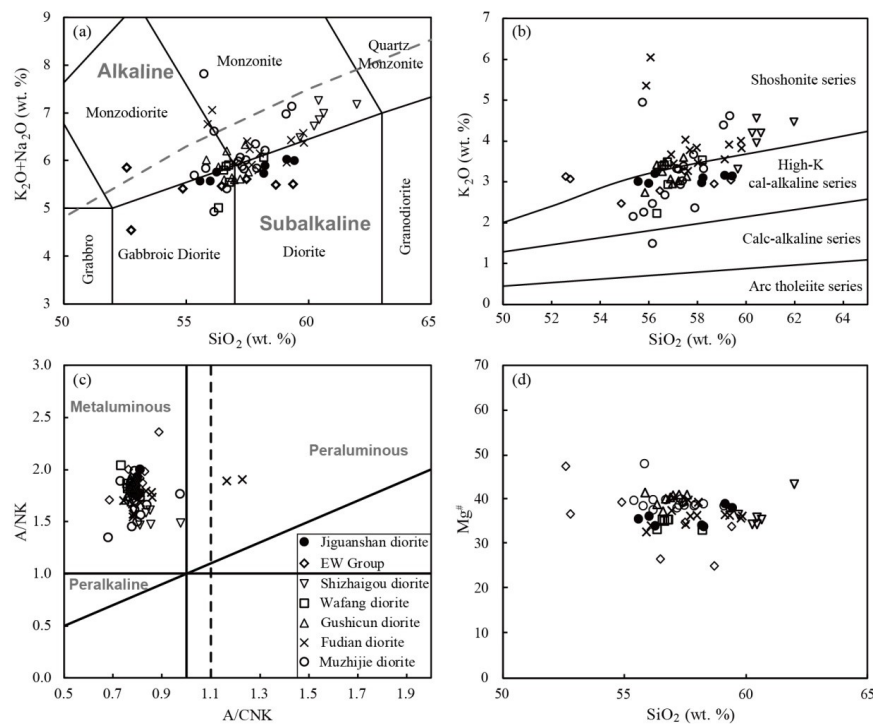


Figure 5 Plots of major elements for the diorites: (a) TAS diagram (after Le Bas et al., 1986); (b) K₂O content versus SiO₂ content (after Peccerillo and Taylor, 1976); (c) A/NK versus A/CNK values (after Maniar and Piccoli, 1989) (d) Mg[#] value versus SiO₂ content (wt. %)

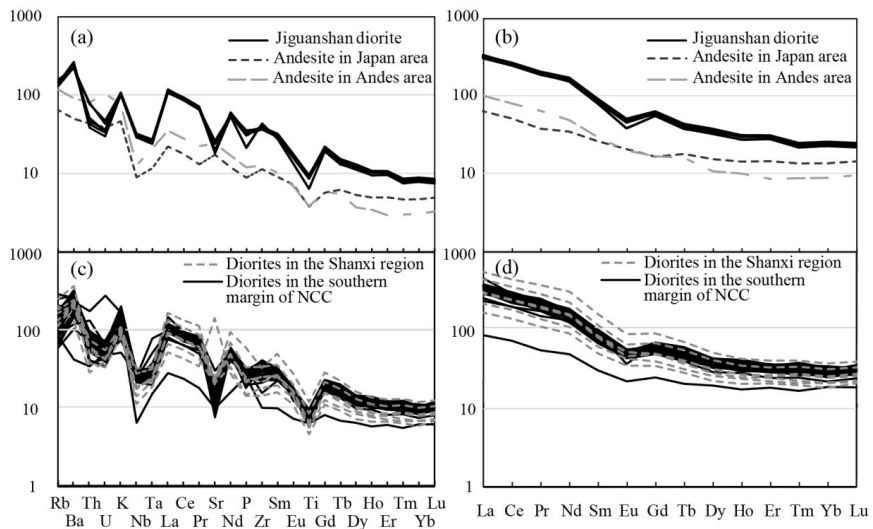




Figure 6 Primitive-mantle normalized trace element spider diagrams and chondrite-normalized REE patterns of diorites. Normalization values from Sun and McDonough (1989); Diorites in Shanxi region (Peng et al., 2007), Diorites in the southern margin of the NCC (Cui et al., 2011; Ma et al 2023a, b; Wang et al., 2016; Zhao et al., 2004). The average trace element compositions of intermediate rocks in the Japan arc and Andes arc are derived from Pan et al. (2017).

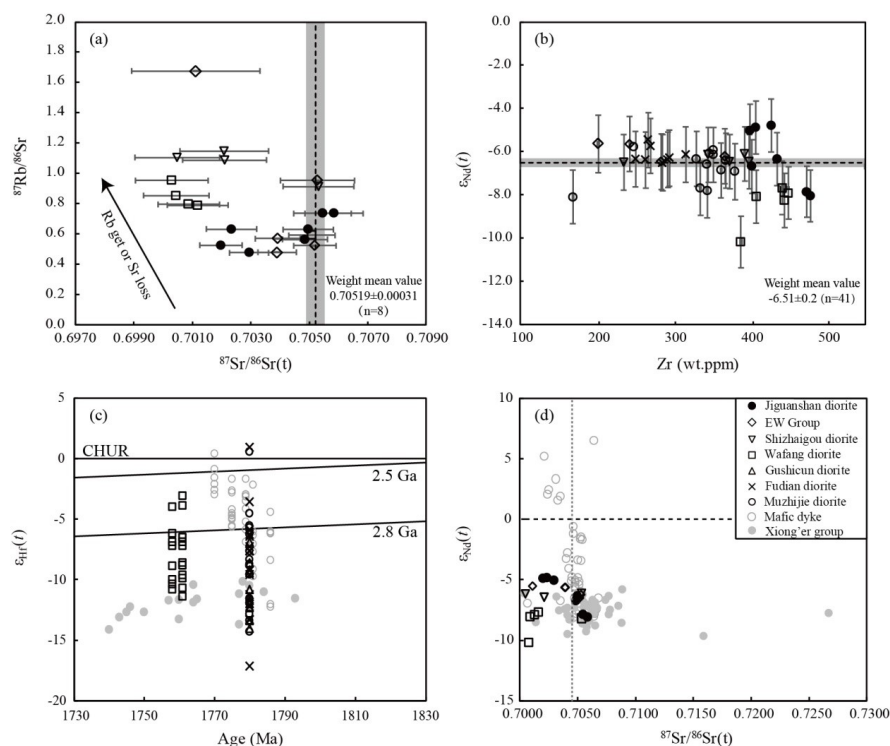


Figure 7 (a) $^{87}\text{Rb}/^{86}\text{Sr}$ value versus $^{87}\text{Sr}/^{86}\text{Sr}(t)$ value; (b) $\epsilon_{\text{Nd}}(t)$ value versus Zr content (ppm); (c) $\epsilon_{\text{Nd}}(t)$ value versus age (Ma); (d) $\epsilon_{\text{Nd}}(t)$ value versus $^{87}\text{Sr}/^{86}\text{Sr}(t)$ value. Data source of the Xiong'er Group (Hf isotope composition, Wang et al., 2010; initial Sr isotope composition and initial ϵ_{Nd} value, He et al., 2008, 2010; Peng et al., 2008; Wang et al., 2010; Zhao et al., 2002); mafic dyke swarms (initial Sr isotope composition and initial ϵ_{Nd} value, Hu et al., 2010; Peng et al., 2007; Wang et al., 2004)

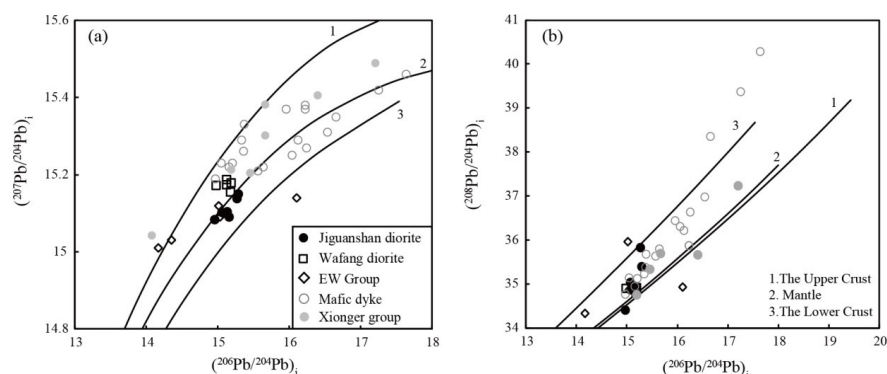


Figure 8 (a) $(^{207}\text{Pb}/^{204}\text{Pb})_i$ versus $(^{206}\text{Pb}/^{204}\text{Pb})_i$; (b) $(^{208}\text{Pb}/^{204}\text{Pb})_i$ versus $(^{206}\text{Pb}/^{204}\text{Pb})_i$. The data source of the Xiong'er Group (Pb isotope composition, Zhao, 2000); mafic dyke swarms (initial Pb isotope composition, Hu et al., 2010; Peng et al., 2007); diorites (initial Pb isotope composition, Peng et al., 2007; Wang et al., 2016)

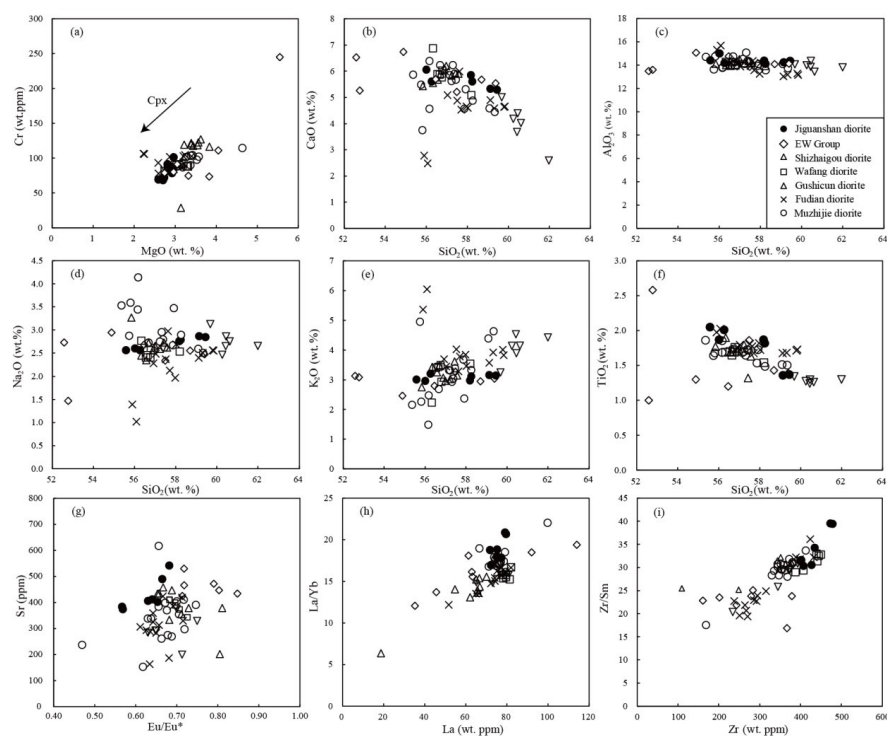
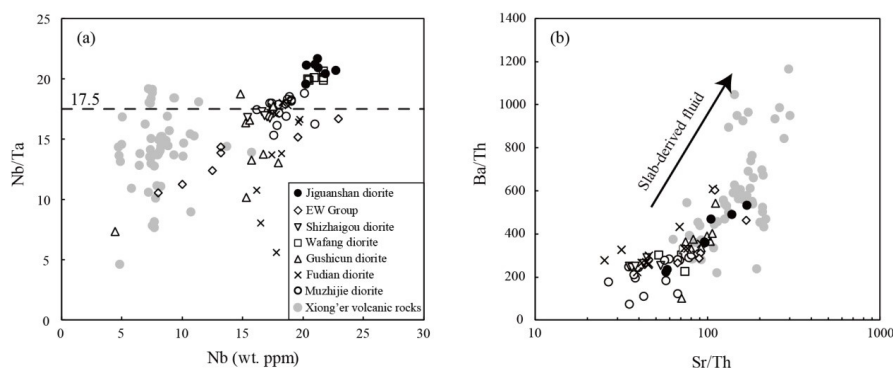


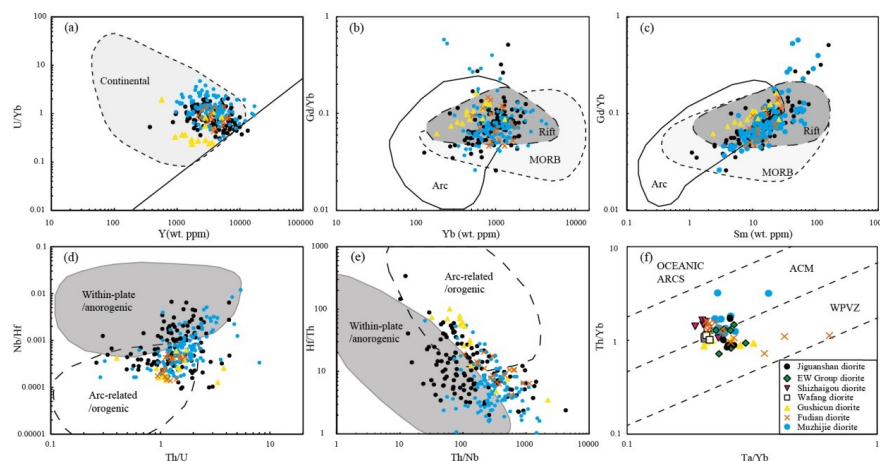
Figure 9 (a) Cr (ppm) content versus MgO content (wt. %); (b) CaO (wt. %) content versus SiO₂ content (wt. %); (c) Al₂O₃ (wt. %) content versus SiO₂ content (wt. %); (d) Na₂O (wt. %) content versus SiO₂ content (wt. %); (e) K₂O (wt. %) content versus SiO₂ content (wt. %); (f) TiO₂ (wt. %) content versus SiO₂ content (wt. %); (g) Sr (ppm) content versus Eu/Eu* ratio; (h) La/Yb ratio versus La (wt. ppm); (i) Zr/Sm ratio versus Zr (wt. ppm)



773 TiO_2 (wt. %) content versus SiO_2 content (wt. %); (g) Eu/Eu^* value versus Sr content (ppm);
774 (h) La/Yb value versus La content (ppm); (i) Zr/Sm value versus Zr content (ppm)



775
776 **Figure 10** (a) Nb/Ta versus Nb content (ppm); (b) Ba/Th value versus Sr/Th values; Data source
777 of the Xiong'er Group (He et al., 2008, 2010; Wang et al., 2010; Zhao et al., 2002)



778
779 **Figure 11** (a) Zircon trace element U/Yb value versus Y (ppm) (after Grimes et al., 2007); (b)
780 Zircon trace element Gd/Yb value versus Yb (ppm) (after Carley et al., 2014); (c) Zircon
781 trace element Gd/Yb value versus Sm (ppm) (after Carley et al., 2014); (d) Zircon trace
782 element Nb/Hf value versus Th/U value (after Hawkesworth and Kemp, 2006); (e) Zircon
783 trace element Hf/Th value versus Th/Nb value (after Yang et al., 2012); (f) Whole-rock trace
784 element Th/Yb value versus Ta/Yb value (after Pearce, 1983; Gorton and Schandl, 2000);



787 **Tables**

788 **Table 1** Major (wt. %) and trace element contents (ppm) of the Jiguanshan diorite

Sample No.	ZY2201	ZY2202	ZY2203	ZY2204	ZY2205	ZY2206	ZY2207
(wt.%)							
SiO ₂	58.18	59.44	59.13	58.24	56.26	56.01	55.57
TiO ₂	1.87	1.37	1.36	1.82	2.01	1.87	2.05
Al ₂ O ₃	14.38	14.37	14.24	14.11	14.18	15.00	14.41
^T Fe ₂ O ₃	10.38	9.04	9.17	10.00	10.35	10.18	10.50
MnO	0.15	0.14	0.14	0.14	0.17	0.14	0.15
MgO	2.73	2.81	2.96	2.59	2.70	2.92	2.94
CaO	5.85	5.29	5.33	5.60	5.61	6.06	5.81
Na ₂ O	2.76	2.85	2.87	2.79	2.56	2.60	2.56
K ₂ O	2.98	3.15	3.16	3.11	3.21	2.97	3.01
P ₂ O ₅	0.71	0.46	0.45	0.65	0.73	0.68	0.76
LOI	0.48	1.31	0.67	0.36	1.53	1.60	1.67
Total	100.47	100.23	99.48	99.41	99.31	100.03	99.43
(ppm)							
Li	11.2	19.8	19.9	14.8	18.6	20.7	18.2
Be	2.66	2.80	2.76	2.94	3.06	2.70	2.97
Sc	22.7	20.1	20.4	23.3	24.3	24.0	23.8
V	163	141	147	168	179	165	164
Cr	72.1	91.3	101.3	69.5	68.6	78.6	83.5
Ni	21.3	22.3	24.0	20.7	19.2	20.2	21.6
Cu	20.8	19.8	19.9	20.9	27.0	22.2	23.3
Zn	131	128	122	133	148	139	141
Ga	21.9	21.9	21.8	22.9	23.3	23.8	22.7
Rb	80.3	95.2	97.8	88.4	88.0	89.5	88.9
Sr	412	374	384	406	403	542	490
Y	47.5	44.4	43.8	48.4	49.3	44.8	46.7
Zr	402	478	474	435	428	400	407
Nb	20.2	21.2	21.0	21.2	22.7	20.3	21.8
Cs	0.60	0.77	0.74	0.95	2.98	3.63	4.44
Ba	1543	1515	1504	1544	1814	1714	1737
La	72.2	79.0	79.5	75.0	77.3	71.7	75.2
Ce	149	161	161	154	163	150	159
Pr	17.6	18.3	18.1	18.2	19.4	18.0	18.9
Nd	72.3	71.2	70.9	73.2	80.0	72.9	77.1
Sm	12.7	12.1	12.0	12.7	14.0	12.8	13.4
Eu	2.63	2.21	2.18	2.59	2.93	2.78	2.87
Gd	12.1	11.2	11.2	12.1	13.0	11.7	12.5
Tb	1.53	1.39	1.40	1.51	1.63	1.47	1.56
Dy	8.99	8.32	8.11	8.92	9.50	8.53	9.00
Ho	1.67	1.54	1.53	1.67	1.75	1.53	1.65
Er	4.97	4.56	4.54	4.95	5.09	4.55	4.87
Tm	0.62	0.55	0.55	0.60	0.63	0.55	0.58



Yb	4.26	3.79	3.84	4.18	4.33	3.82	3.99
Lu	0.61	0.55	0.56	0.60	0.63	0.55	0.58
Hf	7.97	9.09	9.15	8.20	8.46	7.59	7.98
Ta	1.03	0.98	0.99	1.01	1.10	0.96	1.07
Pb	16.4	21.2	18.0	16.3	18.9	15.2	14.2
Th	4.28	6.43	6.71	4.27	3.87	3.22	3.55
U	0.70	0.98	0.88	0.71	0.75	0.61	0.68
<hr/>							
K ₂ O/Na ₂ O	1.08	1.11	1.10	1.11	1.25	1.14	1.18
K ₂ O+Na ₂ O (Wt.%)	5.74	6.00	6.03	5.90	5.77	5.57	5.57
Mg#	34.5	38.3	39.2	34.1	34.3	36.5	35.9
A/CNK	0.78	0.81	0.80	0.78	0.79	0.81	0.80
A/NK	1.85	1.77	1.75	1.77	1.84	2.00	1.93
ΣREE	361.5	375.8	375.1	370.4	393.2	361.2	381.3
Eu/Eu*	0.64	0.57	0.57	0.63	0.65	0.68	0.66
(La/Yb) _N	12.2	15.0	14.8	12.9	12.8	13.5	13.5

789 $Mg^{\#} = (MgO + FeO_{total}) / MgO \times 100$

790 $Eu/Eu^* = 2Eu_N / (Sm_N + Gd_N)$; $(La/Yb)_N$ = chondrite-normalized La/Yb ratio

791



792 **Table 2** Whole-rock Sr isotopic compositions of the late Paleoproterozoic diorites in the NCC

Sample	Age	Rb	Sr	Rb/Sr	⁸⁷ Rb/ ⁸⁶ Sr	⁸⁷ Sr/ ⁸⁶ Sr	±2SE	⁸⁷ Sr/ ⁸⁶ Sr	Error	Data
	(Ma)	(ppm)	(ppm)					(t)	(abs.)	source
Jiguanshan diorite										
ZY2201	1780	80.3	412	0.20	0.5648	0.71931	0.000010	0.70485	0.00077	This study
ZY2202	1780	95.2	374	0.25	0.7371	0.72471	0.000012	0.70584	0.00099	
ZY2203	1780	97.8	384	0.25	0.7377	0.72434	0.000011	0.70546	0.00099	
ZY2204	1780	88.4	406	0.22	0.6307	0.72111	0.000011	0.70496	0.00085	
ZY2205	1780	88.0	403	0.22	0.6334	0.71856	0.000011	0.70235	0.00086	
ZY2206	1780	89.5	542	0.17	0.4780	0.71518	0.000011	0.70294	0.00066	
ZY2207	1780	88.9	490	0.18	0.5252	0.71542	0.000013	0.70198	0.00072	
Wafang diorite										
WF1307-3	1780	107.0	389	0.28	0.7969	0.72131	0.000013	0.70091	0.00106	Wang et al. (2016)
WF1307-4	1780	109.0	400	0.27	0.7895	0.72144	0.000014	0.70123	0.00105	
WF1307-5	1780	84.0	411	0.20	0.5921	0.72024	0.000016	0.70508	0.00080	
WF1307-8	1780	113.0	343	0.33	0.9548	0.72479	0.000016	0.70035	0.00127	
WF1307-9	1780	110.0	373	0.29	0.8545	0.72236	0.000014	0.70048	0.00114	
Shizhaigou diorite										
Ln-1	1780	103.7	272	0.38	1.1040	0.72874	0.000012	0.70048	0.00146	Cui et al. (2011)
Ln-2	1780	101.5	322	0.31	0.9125	0.72868	0.000015	0.70532	0.00121	
Ln-3	1780	136.4	200	0.68	1.9758	0.72509	0.00001	0.67452	0.00259	
Ln-4	1780	116.6	295	0.40	1.1479	0.73149	0.000015	0.70210	0.00152	
Ln-5	1780	112.5	300	0.38	1.0885	0.72997	0.000014	0.70211	0.00144	
E-W Group dyke										
02SX001	1780	154.8	470	0.33	0.9542	0.72970	0.000014	0.70528	0.00127	Peng et al. (2007)
02SX007	1780	81.2	450	0.18	0.5231	0.71858	0.000014	0.70519	0.00072	
03LF01	1780	74.4	449	0.17	0.4801	0.71619	0.000013	0.70390	0.00066	
03FS04	1780	131.8	229	0.58	1.6748	0.74399	0.000012	0.70112	0.00	



									220	
	03FS07	1780	106.0	539	0.20	0.5699	0.71852	0.000013	0.70393	0.00078
	Weight mean value							0.70519	0.00031	(n=8, calculate d by IsoplotR)
793	<hr/>									
	$(^{87}\text{Sr}/^{86}\text{Sr})_s = (^{87}\text{Sr}/^{86}\text{Sr})_0 + (^{87}\text{Rb}/^{86}\text{Sr})_s \times (e^{\lambda t} - 1)$									
794	$\lambda_{^{87}\text{Rb}} = 1.42 \times 10^{-11} \text{ a}^{-1}$									
795	Error of initial ratio is calculated from the measurement error of the isotope ratio, the estimated									
796	concentration error and the age error. The decay constant is considered to be a fixed value.									
797	$\sigma_{\text{Sr}(t)}$ is mean-square deviation of $(^{87}\text{Sr}/^{86}\text{Sr})_t$									
798	σ_{Rb} is mean-square deviation of $(^{87}\text{Rb}/^{86}\text{Sr})_s$									
799	σ_t is mean-square deviation of age									
800	$\sigma_{\text{Sr}(t)} = \sqrt{\sigma_{\text{Sr}}^2 + \sigma_{\text{Rb}}^2 (e^{\lambda t} - 1)^2 + \sigma_t^2 (\lambda e^{\lambda t} (\frac{^{87}\text{Rb}}{^{86}\text{Sr}}))^2}$									
801										



802 **Table 3** Whole-rock Nd isotopic compositions of the late Paleoproterozoic diorites in the NCC

Sample	Age (Ma)	Nd (ppm)	Sm (ppm)	$^{147}\text{Sm}/^{144}\text{Nd}$	$^{143}\text{Nd}/^{144}\text{Nd}$	Error (2s)	$^{143}\text{Nd}/^{144}\text{Nd}(t)$
Jiguanshan diorite							
ZY2201	1780	72.3	12.7	0.1063	0.511238	0.000007	0.509994
ZY2202	1780	71.2	12.1	0.1029	0.511129	0.000008	0.509924
ZY2203	1780	70.9	12.0	0.1022	0.511131	0.000005	0.509934
ZY2204	1780	73.2	12.7	0.1049	0.511240	0.000007	0.510011
ZY2205	1780	80.0	14.0	0.1058	0.511329	0.000007	0.510090
ZY2206	1780	72.9	12.8	0.1058	0.511317	0.000005	0.510078
ZY2207	1780	77.1	13.4	0.1054	0.511320	0.000006	0.510086
E-W Group dyke							
02SX001	1780	113	20.3	0.1084	0.511287	0.000009	0.510018
02SX007	1780	62.6	11.3	0.1093	0.511285	0.000010	0.510005
03LF01	1780	45.1	8.36	0.1120	0.511358	0.000017	0.510047
03FS04	1780	102	17.5	0.1039	0.511270	0.000010	0.510053
03FS07	1780	62.7	11.1	0.1068	0.511297	0.000013	0.510047
Shizhaigou diorite							
Ln-1	1780	69.0	12.3	0.1075	0.511280	0.000012	0.510021
Ln-2	1780	66.4	11.7	0.1065	0.511270	0.000011	0.510023
Ln-3	1780	61.9	11.2	0.1090	0.511280	0.000011	0.510003
Ln-4	1780	71.1	12.6	0.1072	0.511260	0.000011	0.510005
Ln-5	1780	69.4	12.3	0.1072	0.511260	0.000012	0.510005
Wafang diorite							
WF1307-3	1780	78.4	13.7	0.1056	0.511169	0.000008	0.509953
WF1307-4	1780	78.5	14.1	0.1086	0.511215	0.000008	0.509965
WF1307-5	1780	75.9	13.7	0.1091	0.511192	0.000008	0.509936
WF1307-8	1780	77.6	13.4	0.1044	0.511039	0.000007	0.509837
WF1307-9	1780	77.5	13.9	0.1084	0.511193	0.000005	0.509945
Gushicun diorite							
20XRδ-1	1780	58.0	10.9	0.1134	0.511327	0.000004	0.509999
20XRδ-3	1780	63.3	11.7	0.1118	0.511334	0.000006	0.510025
20XRδ-4	1780	59.1	10.9	0.1118	0.511341	0.000006	0.510032
20XRδ-5	1780	53.1	9.9	0.1122	0.511354	0.000006	0.510041



The Muzhijie
diorites

20δPt2-1	1780	63.5	11.5	0.1090	0.511297	0.000004	0.510021
20δPt2-3	1780	64.2	11.7	0.1100	0.511300	0.000004	0.510012
20δPt2-5	1780	66.4	12.3	0.1122	0.511295	0.000007	0.509982
20δPt2-7	1780	72.1	13.1	0.1101	0.511297	0.000008	0.510007
20δPt2-9	1780	54.2	9.6	0.1076	0.511181	0.000006	0.509922
20δPt2-11	1780	64.5	11.4	0.1073	0.511199	0.000006	0.509943
20δPt2-13	1780	62.9	11.2	0.1076	0.511196	0.000008	0.509937
20δPt2-16	1780	67.9	12.3	0.1098	0.511270	0.000007	0.509984

Fudian diorite

20XRSC-1	1780	65.8	12.1	0.1110	0.511309	0.000006	0.510009
20XRSC-2	1780	67.1	12.3	0.1111	0.511315	0.000006	0.510014
20XRSC-3	1780	69.5	12.8	0.1113	0.511314	0.000004	0.510011
20XRSC-4	1780	67.5	12.5	0.1117	0.511311	0.000007	0.510002
20XRSC-5	1780	70.1	12.9	0.1111	0.511311	0.000006	0.510010
20XRSC-6	1780	68.9	12.7	0.1112	0.511324	0.000005	0.510022
20XRSC-8	1780	71.7	12.9	0.1089	0.511331	0.000006	0.510056
20XRSC-9	1780	76.6	13.9	0.1096	0.511325	0.000005	0.510042

Weight mean value

803

804



Error (abs.)	$\epsilon_{Nd}(t)$	Error (ϵ_{Nd})	T_{DM2} (Ga)	Data source
0.000063	-6.69	1.24	2.83	This study
0.000061	-8.04	1.20	2.94	
0.000060	-7.85	1.19	2.93	
0.000062	-6.35	1.22	2.80	
0.000063	-4.80	1.23	2.68	
0.000063	-5.03	1.23	2.70	
0.000062	-4.88	1.22	2.68	
0.000065	-6.21	1.27	2.79	Peng et al. (2007)
0.000065	-6.47	1.28	2.81	
0.000068	-5.64	1.34	2.75	
0.000062	-5.53	1.22	2.74	
0.000064	-5.65	1.26	2.75	
0.000065	-6.15	1.26	2.79	Cui et al. (2011)
0.000064	-6.10	1.25	2.78	
0.000065	-6.50	1.28	2.82	
0.000064	-6.46	1.26	2.81	
0.000064	-6.46	1.26	2.81	
0.000062	-7.90	1.23	2.93	Wang et al. (2016)
0.000063	-7.67	1.26	2.91	
0.000064	-8.24	1.27	2.96	
0.000061	-10.2	1.21	3.11	
0.000063	-8.07	1.26	2.94	
0.000067	-6.58	1.31	2.82	Ma et al. (2023a)
0.000066	-6.08	1.30	2.78	
0.000066	-5.94	1.30	2.77	
0.000066	-5.77	1.30	2.76	
0.000064	-6.15	1.26	2.79	Ma et al. (2023b)



0.000065	-6.33	1.27	2.80
0.000067	-6.92	1.30	2.85
0.000065	-6.42	1.28	2.81
0.000064	-8.09	1.25	2.95
0.000064	-7.69	1.25	2.91
0.000064	-7.80	1.25	2.92
0.000065	-6.87	1.28	2.85

0.000066	-6.39	1.29	2.81
0.000066	-6.30	1.29	2.80
0.000066	-6.35	1.29	2.80
0.000066	-6.52	1.30	2.82
0.000066	-6.37	1.29	2.81
0.000066	-6.14	1.29	2.79
0.000065	-5.46	1.26	2.75
0.000065	-5.74	1.27	2.75

Ma et al. (2023b)

-6.51 0.20 (n=41, calculated by IsoplotR)

$$({}^{143}\text{Nd}/{}^{144}\text{Nd})_s = ({}^{143}\text{Nd}/{}^{144}\text{Nd})_0 + ({}^{147}\text{Sm}/{}^{144}\text{Nd})_s \times (e^{\lambda t} - 1)$$

$$\varepsilon_{\text{Nd}}(t) = [({}^{143}\text{Nd}/{}^{144}\text{Nd})_t / ({}^{143}\text{Nd}/{}^{144}\text{Nd})_{\text{CHUR}(t)} - 1] \times 10000$$

$$T_{\text{DM2}} = 1/\lambda \times \ln \{ 1 + [({}^{143}\text{Nd}/{}^{144}\text{Nd})_{\text{DM}} - ({}^{143}\text{Nd}/{}^{144}\text{Nd})_s + (({}^{147}\text{Sm}/{}^{144}\text{Nd})_s - ({}^{147}\text{Sm}/{}^{144}\text{Nd})_{\text{CC}}) \times (e^{\lambda t} - 1)] \}$$

$$\varepsilon_{\text{Nd}}(t) = [({}^{143}\text{Nd}/{}^{144}\text{Nd})_t / ({}^{143}\text{Nd}/{}^{144}\text{Nd})_{\text{CHUR}(t)} - 1] \times 10000 / (({}^{147}\text{Sm}/{}^{144}\text{Nd})_{\text{DM}} - ({}^{147}\text{Sm}/{}^{144}\text{Nd})_{\text{CC}})$$

$$\lambda_{147\text{Sm}} = 0.654 \times 10^{-11} \text{ a}^{-1}$$

$$({}^{143}\text{Nd}/{}^{144}\text{Nd})_{\text{DM}} = 0.51315$$

$$({}^{147}\text{Sm}/{}^{144}\text{Nd})_{\text{DM}} = 0.2137$$

$$({}^{147}\text{Sm}/{}^{144}\text{Nd})_{\text{CC}} = 0.12$$

Error of initial ratio is calculated from the measurement error of the isotope ratio, the estimated concentration error and the age error. The decay constant is considered to be a fixed value.

$\sigma_{\text{Nd}(t)}$ is mean-square deviation of $({}^{143}\text{Nd}/{}^{144}\text{Nd})_t$

σ_{Sm} is mean-square deviation of $({}^{147}\text{Sm}/{}^{144}\text{Nd})_s$

σ_t is mean-square deviation of age

$$\sigma_{\text{Nd}(t)} = \sqrt{\sigma_{\text{Nd}}^2 + \sigma_{\text{Sm}}^2 (e^{\lambda t} - 1)^2 + \sigma_t^2 (\lambda e^{\lambda t} (\frac{{}^{147}\text{Sm}}{{}^{144}\text{Nd}}))^2}$$



820 **Table 4** Whole-rock Pb isotopic compositions of the Jiguanshan diorite

Spon.no	U (ppm)	Th (ppm)	Pb (ppm)	$^{206}\text{Pb}/^{204}\text{Pb}$	$\pm 2\text{SE}$	$^{207}\text{Pb}/^{204}\text{Pb}$	$\pm 2\text{SE}$
ZY2201	0.70	4.28	16.38	15.867	0.0005	15.189	0.0005
ZY2202	0.98	6.43	21.20	16.167	0.0008	15.243	0.0009
ZY2203	0.88	6.71	18.03	15.882	0.0006	15.182	0.0006
ZY2204	0.71	4.27	16.29	16.097	0.0010	15.225	0.0009
ZY2205	0.75	3.87	18.90	15.832	0.0007	15.179	0.0006
ZY2206	0.61	3.22	15.22	15.914	0.0010	15.170	0.0010
ZY2207	0.68	3.55	14.22	16.036	0.0008	15.199	0.0007

821

822



$^{208}\text{Pb}/^{204}\text{Pb}$	$\pm 2\text{SE}$	$^{206}\text{Pb}/^{204}\text{Pb}$	$^{207}\text{Pb}/^{204}\text{Pb}$	$^{208}\text{Pb}/^{204}\text{Pb}$	$^{238}\text{U}/^{204}\text{Pb}$	$^{232}\text{Th}/^{204}\text{Pb}$	$^{232}\text{Th}/^{238}\text{U}$
		initial	initial	initial	μ	ω	
36.502	0.0014	15.063	15.103	35.027	2.6	16.0	6.3
37.126	0.0022	15.295	15.150	35.392	2.8	18.8	6.8
36.494	0.0013	14.965	15.084	34.398	2.9	22.8	7.8
37.324	0.0023	15.271	15.137	35.825	2.6	16.3	6.2
36.046	0.0016	15.095	15.100	34.901	2.3	12.4	5.3
36.124	0.0024	15.164	15.090	34.939	2.4	12.9	5.4
36.338	0.0016	15.136	15.103	34.931	2.9	15.3	5.4

823 Initial Pb isotopic ratios are calculated back to 1780 Ma.

824



825 **Supplementary material/Appendix:**

826 **Table S1** Zircon U–Pb isotopic data for the Jiguanshan diorite obtained by the LA-ICP-MS
827 technique

828 **Table S2** Zircon trace element data for the Jiguanshan diorite obtained by the LA-ICP-MS
829 technique

830